

***P* and *S* receiver function analysis of seafloor borehole broadband seismic data**

P. Kumar,^{1,2} H. Kawakatsu,¹ M. Shinohara,¹ T. Kanazawa,¹ E. Araki,³ and K. Suyehiro³

Received 4 May 2011; revised 29 September 2011; accepted 5 October 2011; published 14 December 2011.

[1] The crustal and lithospheric structure of the normal oceanic plates is investigated using converted wave techniques (*P* and *S* receiver functions (RFs) and novel stacking analysis techniques without deconvolution) applied to the data from two seafloor borehole broadband seismic stations located in the central Philippine Sea and in the northwest Pacific ocean. We observe sufficient energy from at least two discontinuities within the error bounds, one from the crust-mantle (Moho) boundary and the other from the seismic lithosphere-asthenosphere boundary (LAB). Synthetic seismograms for seafloor stations show that the water reverberations interfere with the vertical component of seismograms but to a lesser extent with the radial part of *P* receiver functions. On the other hand, *S* receiver functions are devoid of such effects since all the multiples and converted waves are separated in time by the primary *S* wave in time. Waveform modeling of RFs shows that the crustal thicknesses of the western Philippine Sea plate and northwest Pacific plate are ~ 7 – 8 km, and that depths of LAB are 76 ± 1.8 km and 82 ± 4.4 km, respectively, with an abrupt *V_s* drop at LAB of $\sim 7\%$ – 8% , as reported by Kawakatsu *et al.* (2009). The LAB depth for the eastern Philippine plate is found to be ~ 55 km. To confirm the robustness of this observation, we further analyze vertical and radial components of the data without deconvolution for *P* wave backscattered reflection phases and *P*-to-*S* converted phases. The result indicates that the reflected/converted phases from Moho and LAB are observed at timings consistent with the receiver function results. The effect of seismic anisotropy for observed RFs is also investigated.

Citation: Kumar, P., H. Kawakatsu, M. Shinohara, T. Kanazawa, E. Araki, and K. Suyehiro (2011), *P* and *S* receiver function analysis of seafloor borehole broadband seismic data, *J. Geophys. Res.*, 116, B12308, doi:10.1029/2011JB008506.

1. Introduction

[2] Delineating the structure of the oceanic crust and uppermost mantle (say, down to ~ 250 km) is essential for our understanding of plate tectonics, and a great deal of efforts have been made by various researchers. The most straightforward but challenging approach involves deploying ocean bottom seismometers to register seismic waves generated by active and passive seismic sources [e.g., Raitt, 1963; Spudich and Orcutt, 1980; Shinohara *et al.*, 2008], and significant progress has been made in deciphering the structure of the oceanic crust and the subcrustal mantle [e.g., White *et al.*, 1992; Shearer and Orcutt, 1986; Shimamura and Asada, 1984]; however, because of noisy conditions on the seafloor, the limited frequency range of seismic sensors, and/or the limited energy of seismic excitation sources, only rays traveling through the subcrustal mantle have been

analyzed, limiting the resolution below this depth range. Approaches using long-period seismic surface waves have complemented the situation, as they sense the deep structures depending on the frequency range analyzed, and have been successful in establishing age-dependent structures and the presence of the low-velocity zone (LVZ) of the oceanic upper mantle [e.g., Oliver, 1962; Kanamori and Press, 1970; Leeds *et al.*, 1974; Forsyth, 1975; Zhang and Tanimoto, 1993; Ekström and Dziewonski, 1998; Nettles and Dziewonski, 2008]; it is, however, the inherent nature of surface wave studies that do not offer detailed depth resolution as compared to body waves. It is, therefore, not easy to distinguish different existing models for the oceanic upper mantle (say, lithosphere-asthenosphere system) proposed by various researchers in various fields of geoscience [e.g., Anderson and Sammis, 1970; Anderson, 1995; Hirth and Kohlstedt, 1996; Karato and Jung, 1998; Faul and Jackson, 2005; Priestley and McKenzie, 2006; Holtzman and Kohlstedt, 2007].

[3] Observation of reflected/converted seismic phases from possible sharp boundaries in the oceanic uppermost mantle would significantly contribute to our understanding of the processes controlling plate tectonics; for example, if a presence of a sharp seismic discontinuity is confirmed at the

¹Earthquake Research Institute, University of Tokyo, Tokyo, Japan.

²National Geophysical Research Institute, Council of Scientific and Industrial Research, Hyderabad, India.

³Japan Agency for Marine-Earth Science and Technology, Yokosuka, Japan.

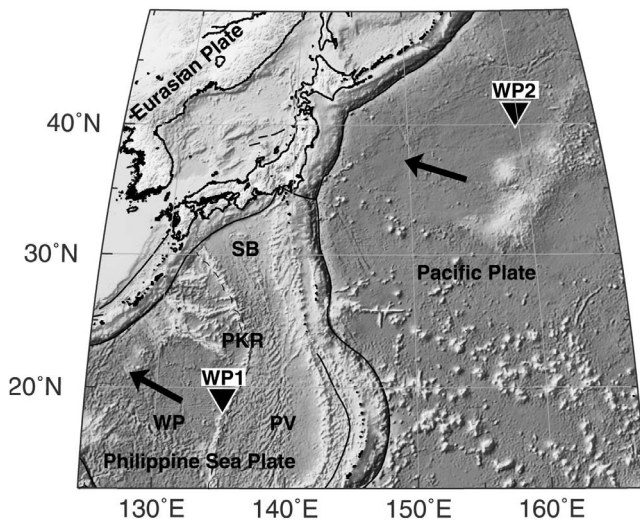


Figure 1. Topographic map showing the location of seafloor borehole broadband seismic stations (inverted triangles): WP1 in the Philippine Sea and WP2 in the northwest Pacific. Palau Kyushu Ridge (PKR) runs almost in the center of the Philippine Sea plate from north to south and divides the plate into three distinct geological provinces: PV, Parece-Vela basin (15–27 Myr); WP, Western Philippine basin (33–49 Myr); SB, Shikoku basin. The arrows denote the present-day plate motion directions.

top of the LVZ, it would strongly imply that the origin of LVZ cannot be attributed solely to thermal or pressure effects, as these factors affect the seismic velocity gradually not making a sharp boundary; other factors, such as partial melt or a change in chemical composition may be invoked. *Revenaugh and Jordan* [1991a, 1991b] introduced an innovative approach for the purpose, and their *ScS* reverberation technique resolved boundaries with a significant velocity reduction (from shallow to deep) in the oceanic area. The so-called G discontinuity, after Gutenberg who first suggested a low-velocity channel in a depth range of ~50–200 km [e.g., *Gutenberg*, 1959], is observed in Pacific around depths of 50–100 km [*Revenaugh and Jordan*, 1991b]. There are, however, a few drawbacks in the method; first the method usually uses *ScS*-related phases that sample large spatial distance, and thus obtained result is a spatial average of points separated by thousands of kilometers; second, because of the similarity in ray geometry, the structure obtained could be due, instead of the top of the mantle, to the bottom of the mantle (CMB) which is known to be highly heterogeneous; third because of the long-period (~35 s) nature of *ScS* phases, the method is sensitive even to a transition thickness as wide as ~40 km [*Richards*, 1972; *Revenaugh and Jordan*, 1991a] which may be too wide to discriminate different models of the lithosphere-asthenosphere system. Precursors to other global phases such as *SS* and *PP* have been often used to map discontinuities of the upper mantle [*Shearer*, 1991], but application to the structure above 100 km depth is challenging (though should not be impossible) as the separation from the reference phases becomes small [*Gu et al.*, 2001; *Deuss and Woodhouse*, 2002; *Rychert and Shearer*, 2011].

[4] The station-based methods that retrieve structural information just beneath seismic stations, such as the receiver function technique [e.g., *Vinnik*, 1977] or the shear wave splitting technique [e.g., *Ando et al.*, 1983], are getting more and more common with the spread of permanent-temporal broadband seismic networks. In the ocean, significant progress has been made and temporal, yet long-term (say, over 1 year) deployment of broadband ocean bottom seismometers (BBOBSs) has become possible [e.g., *Shiobara et al.*, 2009]; BBOBSs are, however, still at a developing stage and the presence of high-amplitude noise in the horizontal components hampers the application of aforementioned station-based methods for the detailed structure of the uppermost mantle beneath ocean. There are studies utilizing data from ocean islands [e.g., *Li et al.*, 2004; *Rychert and Shearer*, 2009], however, the structures derived from ocean islands may not be a proxy for normal oceanic plates. It is thus highly desirable that we have seismic deployments comparable in noise quality to the continental condition that allow us to employ seismic analysis techniques commonly used for continental areas.

[5] Under the Ocean Hemisphere network Project (OHP), Japanese scientists have deployed broadband seismometers in two seafloor borehole seismic observatories located in the Philippine Sea and the northwest Pacific [*Kanazawa et al.*, 2001; *Fukao et al.*, 2001; *Salisbury et al.*, 2002; *Araki et al.*, 2004; *Shinohara et al.*, 2006, 2008]. We analyze data from these stations to investigate the seismic structure of the normal oceanic mantle. Emplacing seismometers in deep boreholes greatly reduces the noise in the horizontal components as well as in the vertical one, and thus allows us to apply the station-based methodology. The seismic structures derived from these seafloor borehole seismic stations are truly oceanic, and are of essential importance for our understanding of plate tectonics.

[6] We employ the receiver function analysis that is commonly used to retrieve crustal and upper mantle seismic parameters from three-component seismograms [e.g., *Burdick and Langston*, 1977; *Langston*, 1977; *Vinnik*, 1977]. The *P* receiver function (PRF) technique utilizes *P*-to-*s* conversions from a discontinuity beneath the seismic station. In recent times a new technique has emerged, namely, the *S* receiver function (SRF) technique [*Farra and Vinnik*, 2000] that looks for the *S*-to-*p* conversions from discontinuities. We use both techniques to look for seismic discontinuities in the uppermost mantle. We particularly focus on a structure often referred to as the lithosphere-asthenosphere boundary (LAB), a rapid seismic velocity reduction in the depth range of 50–200 km reported by various workers utilizing SRFs in diverse tectonic regimes of the world [e.g., *Li et al.*, 2004; *Kumar et al.*, 2005a, 2005b, 2006, 2007; *Soudoudi et al.*, 2006; *Angus et al.*, 2006; *Landes et al.*, 2007; *Rychert et al.*, 2007].

[7] The seismic LAB may be identified with the G discontinuity observed in the ocean by *Revenaugh and Jordan* [1991b] that may define a boundary between seismic lid and LVZ. The usage of the word LAB, however, seems to require some caution, as the so-called LAB just represents a sharp velocity boundary observed by seismological means, and may not necessarily correspond to the mechanical/dynamical boundary between lithosphere and asthenosphere called for by plate tectonics [e.g., *Anderson*, 1995]. With these cautions in mind, nevertheless in this paper, we still use the word LAB

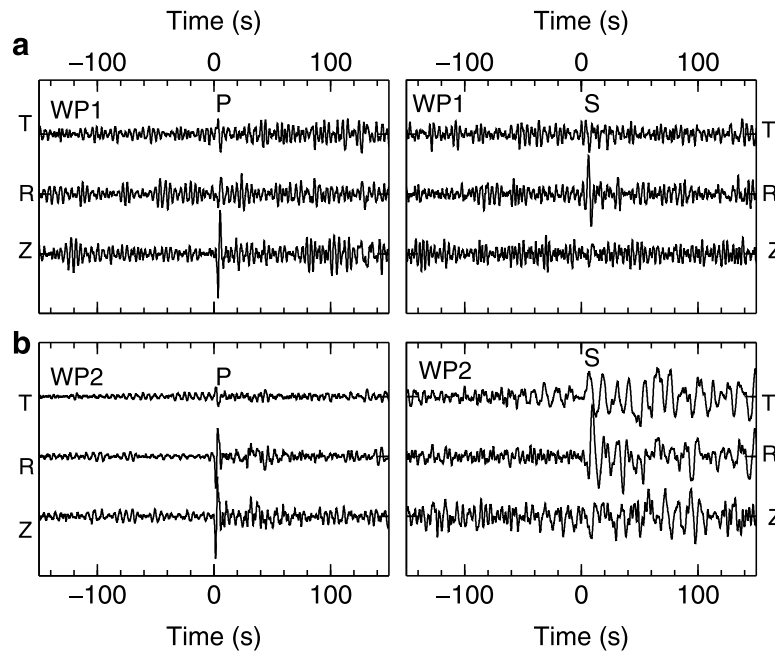


Figure 2. An example of three component teleseismic waveforms recorded at station (a) WP1 and (b) WP2. (left) P wave window. (right) S wave window. Zero time indicates the theoretical onset of primary P and S waves based on the IASP91 model.

to refer to the structure determined seismologically, partly because we cannot find a good alternative and partly to be consistent with our earlier papers. In future literature, this point may be straightened out.

[8] Two seafloor borehole broadband seismic stations are located in the Philippine Sea (station WP1) and in the north-west Pacific ocean (WP2). The upper mantle discontinuities have been studied using the data from WP1 by *Suetsugu et al.* [2005] and for WP2 the crustal and mantle discontinuities were studied by *Shinohara et al.* [2008]. Recently, *Kawakatsu et al.* [2009a] used these data to show the presence of seismic LABs beneath the normal ocean, along with the image of the LAB of the subducting Pacific slab from the analysis of the dense

seismic network data from Japan. In the present paper, we first give a full description of the analyses of the seafloor borehole broadband seismic data by *Kawakatsu et al.* [2009a] in section 3 with additional information, and further demonstrate the robustness of the observations using a new technique that does not involve deconvolution as required for the conventional receiver function analyses (section 4).

2. Data and Methodology

[9] The seafloor borehole seismic observatories WP1 in Philippine Sea and WP2 in western Pacific are deployed under the Japanese Ocean Hemisphere network Project

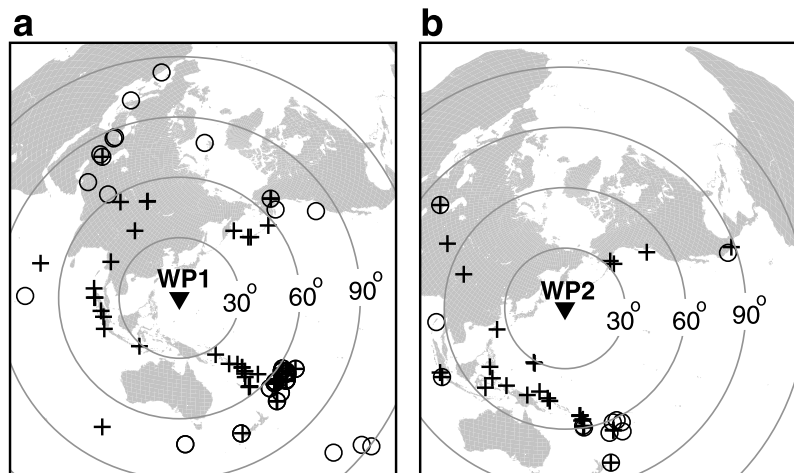


Figure 3. Distribution of earthquakes used in the present study. Inverted triangles are the location of seafloor borehole broadband seismic observatories, namely, (a) WP1 and (b) WP2. Crosses and open circles are the events used for P and S waves, respectively. A few SKS waves were also used. Concentric circles are plotted with equal epicentral distances from the stations.

Table 1. WP1 *P* Wave

Origin Time	Latitude (deg)	Longitude (deg)	Depth (km)	m_b
2002-04-11_21:56:56.390	-14.39	167.69	10	5.9
2002-04-20_15:59:57.890	-16.38	173.26	33	6.0
2002-05-08_05:26:00.400	-17.95	-174.57	130.8	5.4
2002-05-15_03:27:35.590	-21.41	-174.26	10	5.4
2002-06-13_01:27:19.500	-47.8	99.75	10	5.5
2002-06-16_18:31:10.790	-2.34	102.56	231.6	5.4
2002-06-17_21:26:22.890	-12.59	166.38	33	6.0
2002-08-19_11:01:01.199	-21.7	-179.51	580	6.7
2002-06-21_14:21:44.890	-15.11	-175.86	318.6	5.7
2002-06-22_02:58:21.290	35.63	49.05	10	6.2
2002-06-27_05:50:35.090	-6.96	104.18	11	6.0
2002-06-29_02:39:00.700	-12.4	166.52	33	5.9
2002-08-09_13:31:05.300	-16.31	-176.17	364.1	5.5
2002-10-04_19:05:48.790	-20.99	-179.02	621.1	6.1
2002-10-22_11:39:04.199	-20.63	-178.39	549	5.5
2002-10-23_11:27:19.390	63.51	-147.91	4.2	6.0
2002-10-24_21:53:43.200	6.03	94.42	64.6	6.2
2002-11-02_01:26:10.700	2.82	96.08	30	6.2
2002-11-02_09:46:46.690	2.95	96.39	27	5.9
2002-11-03_22:12:41.000	63.52	-147.44	4.9	7.0
2003-01-04_05:15:03.800	-20.57	-177.66	378	6.0
2003-01-20_08:43:06.099	-10.49	160.77	33	6.7
2003-02-19_03:32:36.400	53.65	-164.64	19	5.8
2003-02-24_02:03:41.500	39.61	77.23	11	5.8
2003-03-25_02:53:25.000	-8.29	120.74	33	6.2
2003-04-17_00:48:38.600	37.53	96.48	14	6.2
2003-05-04_13:15:18.690	-30.53	-178.23	62.4	6.0
2003-05-04_20:08:46.500	-30.59	-178.29	45.6	6.0
2003-05-13_21:21:14.100	-17.29	167.74	33	6.0
2003-06-12_08:59:20.190	-5.99	154.76	186.3	5.9
2003-06-23_12:12:34.500	51.44	176.78	20	6.3
2003-07-03_06:21:50.400	-21.28	-174.52	10	5.5
2003-07-06_21:34:15.390	-15.58	167.53	86.2	5.3
2003-07-07_16:30:08.300	-21.93	-179.5	595.3	5.0
2003-07-14_20:00:06.296	-0.54	100.82	144.2	5.4
2003-07-15_20:27:50.500	-2.6	68.38	10	6.1
2003-07-27_02:04:11.500	-21.08	-176.59	212.9	5.9
2003-08-14_18:23:06.296	-19.9	-177.98	563.3	5.2
2003-08-21_12:12:49.800	-45.1	167.14	28	6.6
2003-09-21_18:16:13.390	19.92	95.67	10	6.1
2003-09-27_11:33:25.100	50.04	87.81	16	6.5
2003-10-01_01:03:25.190	50.21	87.72	10	6.3
2003-10-06_18:29:38.290	-10.75	164.42	33	5.5
2003-10-07_04:55:28.800	-16.53	-170.19	10	6.2
2003-11-17_06:43:06.800	51.15	178.65	33	6.2
2003-12-05_21:26:09.500	55.54	165.78	10	6.1
2003-12-25_20:42:33.700	-22.25	169.49	10	6.3
2003-12-26_21:26:04.101	-22.27	169.31	10	6.1
2003-12-27_16:00:59.500	-22.01	169.77	10	6.1
2004-01-03_16:23:21.000	-22.25	169.68	22	6.4
2004-01-25_11:43:11.890	-16.83	-174.2	129.8	6.4

(OHP) [Fukao *et al.*, 2001; Kanazawa *et al.*, 2001; Araki *et al.*, 2004; Shinohara *et al.*, 2006, 2008]. The location of these stations is shown in Figure 1. Both of the stations are deployed in boreholes on the seafloor. The borehole depths are ~460 m and ~561 m below the ocean floor for WP1 and WP2, respectively. The thickness of the ocean water column at WP1 site is 5710 m while that at WP2 site is 5566 m. The details of the operation, installations, data quality and noise levels are described by Shinohara *et al.* [2006]. From both of the stations, data for about 400 days were retrieved.

[10] Figure 2 shows examples of data used in our present analysis. The data from the teleseismic distance range (for *P* waves, 30°–90°; *S* waves, 60°–85°; and *SKS* waves, 85°–120°; Figure 3) with a magnitude (m_b) greater than ~5.5 are

selected from all the available back azimuths. Further the waveforms are visually inspected for *S* phase in radial components, and only those which show good *SV* arrivals are retained for SRFs. *P* phases in vertical components are also inspected for PRFs. The waveforms are then filtered with a low-pass filter with corner frequencies of 1 Hz for *P* wave data and 0.25 Hz for *S* wave data. For *P* waves we got 51 and 30 events for WP1 and WP2, respectively, while for *S* wave analysis of WP1 data we have only 16 events for the West Philippine and 19 events for the Parece-Vela basin (Figure 1). For WP2 we have only 12 events (Tables 1–4).

[11] Waveforms of each event are then rotated into radial and transverse components using the back azimuth information. While making radial and transverse components, we take care of the original misalignments of the horizontal components by using the North direction derived from the air gun shooting experiments carried out near the stations [Shinohara *et al.*, 2008]. Finally, we derive the radial receiver functions of PRF by deconvolving the radial components by their respective vertical ones in time domain. Here we use the radial component of PRF in order to minimize the effect of water reverberations (see section 3.2 for more discussion) at the cost of obscuring the main *P* and *Pms* (conversion from Moho). However, the latter problem can be overcome by systematic modeling using accurate crustal parameters (crustal parameters are used from the reflection-refraction studies of Shinohara *et al.* [2006]).

[12] For computation of the SRF, on the other hand, we further rotate the vertical and radial components into *P* and *SV* using the angle of incidence. The steps we follow here to compute the SRF are described elsewhere [Kumar *et al.*,

Table 2. WP2 *P* Wave

Origin Time	Latitude (deg)	Longitude (deg)	Depth (km)	m_b
2000-07-16_17:25:23.100	-12.4	166.51	33	5.3
2000-07-24_12:17:26.500	-5.56	102.89	33	5.4
2000-11-16_04:54:56.690	-3.98	152.17	33	6.0
2000-11-16_07:42:16.900	-5.23	153.1	30	6.2
2000-12-18_01:19:21.600	-21.18	179.12	628.2	6.4
2001-01-09_16:49:28.000	-14.93	167.17	103	6.3
2001-08-21_06:52:06.199	-36.81	179.57	33	6.4
2001-08-27_01:16:47.500	1.09	126.36	33	5.8
2001-08-29_17:57:24.000	57.85	155.65	105.1	5.1
2001-09-11_14:56:50.890	-0.58	133.13	33	5.8
2001-09-12_08:48:37.300	-20.99	179.11	608.1	5.7
2001-09-12_22:24:54.000	48.72	128.64	10	5.0
2001-09-22_06:48:06.099	55.83	154.47	33	4.9
2001-09-29_02:40:07.400	-18.5	168.16	33	5.5
2001-10-07_02:21:09.799	-3.3	142.93	10	5.7
2001-10-12_15:02:16.800	12.69	144.98	37	6.7
2001-10-19_03:28:44.500	-4.1	123.91	33	6.3
2001-11-14_09:26:10.000	35.95	90.54	10	6.1
2001-12-18_04:02:58.290	23.95	122.73	14	6.3
2002-01-02_17:22:48.800	-17.6	167.86	21	6.3
2002-03-03_12:08:07.800	36.43	70.44	209	6.3
2002-03-05_21:16:09.101	6.03	124.25	31	6.3
2002-04-11_21:56:56.390	-14.39	167.69	10	5.9
2002-04-26_16:06:07.000	13.09	144.62	85.7	6.5
2002-06-06_23:53:48.500	-0.88	148.33	10	5.7
2002-06-17_21:26:22.890	-12.59	166.38	33	6.0
2002-06-19_21:50:08.296	16.33	-97.94	33	5.2
2002-06-22_02:58:21.290	35.63	49.05	10	6.2
2002-06-27_05:50:35.090	-6.96	104.18	11	6.0
2002-06-29_02:39:00.700	-12.4	166.52	33	5.9

Table 3. WP1 *S* Wave

Origin Time	Latitude (deg)	Longitude (deg)	Depth (km)	m_b
2002-04-08_03:48:55.200	-51.07	139.27	10	5.6
2002-04-12_04:00:23.700	35.96	69.42	10	5.8
2002-04-24_11:00:00.898	-56.13	-122.31	10	5.6
2002-05-08_05:26:00.400	-17.95	-174.57	130.8	5.4
2002-06-07_12:09:40.890	-26.73	-176.69	33	4.9
2002-06-21_14:21:44.890	-15.11	-175.86	318.6	5.7
2002-06-22_02:58:21.290	35.63	49.05	10	6.2
2002-07-28_17:16:31.100	37.93	20.69	22.2	4.8
2002-08-19_11:01:01.199	-21.7	-179.51	580	6.7
2002-08-19_11:08:24.300	-23.88	178.49	675.4	7.0
2002-08-09_13:31:05.300	-16.31	-176.17	364.1	5.5
2002-09-05_03:38:39.090	58.17	-151.45	47.2	5.0
2002-10-04_19:05:48.790	-20.99	-179.02	621.1	6.1
2002-10-18_11:16:48.300	-57.19	-142.75	10	5.1
2002-10-23_11:27:19.390	63.51	-147.91	4.2	6.0
2002-12-24_17:03:02.898	34.59	47.45	33	5.1
2003-01-16_02:25:05.099	44.28	-129.35	10	5.2
2003-01-27_05:26:23.000	39.5	39.88	10	5.6
2003-04-02_21:31:38.000	-25.12	179.9	498	5.4
2003-04-11_05:01:30.300	-15.4	67.26	10	5.4
2003-04-17_03:46:43.000	-55.27	-128.92	10	4.9
2003-04-18_23:32:04.398	-17.76	-173.87	33	5.2
2003-05-01_00:27:04.699	39.01	40.46	10	5.7
2003-05-04_13:15:18.690	-30.53	-178.23	62.4	6.0
2003-05-04_20:08:46.500	-30.59	-178.29	45.6	6.0
2003-05-22_13:57:20.600	37.03	3.93	10	4.9
2003-07-03_06:21:50.400	-21.28	-174.52	10	5.0
2003-07-04_07:16:44.690	76.37	23.28	10	5.7
2003-07-27_02:04:11.500	-21.08	-176.59	212.9	5.9
2003-10-07_04:55:28.800	-16.53	-170.19	10	6.2
2003-11-02_05:32:15.690	-45.19	166.54	10	5.3
2003-12-26_01:56:52.390	29	58.31	10	6.0
2004-01-11_08:07:05.000	-16.24	-176.18	366.1	5.3
2004-01-25_11:43:11.890	-16.83	-174.2	129.8	6.4
2004-01-29_20:10:41.390	-20.82	-174.16	12	5.1

2005a, 2005b, 2006; *Kumar and Kawakatsu, 2011*], and can be briefly stated as follow: first, all the seismograms are aligned by its primary phases (in this case, *S* wave) using the theoretical *S* onset time based on IASP91 model. Then we cut the data, say, hundreds before and after the reference phase. The *Z* and *R* components of the mantle *S* phases are rotated into a local ray coordinate system corresponding to the *P* and *SV* wave polarization directions. The incidence angle for the rotation was determined by minimizing the amplitudes of *P* components at *S* arrival times. Second, the converted *Sp* phases arrive earlier than the primary *S* phase and their conversion coefficients are negative, so for the sake of comparison with PRF, we reverse the time scale and change the polarity of SRF [*Kumar et al., 2005a, 2005b, 2006; Yuan et al., 2006*]. Finally, to enable easy comparison of *Sp* and *Ps* times at a station, we applied the same moveout correction to both types of data with a reference slowness of 6.4 s/deg [*Yuan et al., 1997*] using IASP91 model.

3. Analyses of *Kawakatsu et al. [2009a]*

3.1. Receiver Function Analysis

[13] Figure 4 shows the moveout corrected stacked PRFs and SRFs with respective radial and *P* components for stations WP1 (Figure 4a) and WP2 (Figure 4b). Since *S*-to-*p* conversions have larger lateral extent due to their larger slowness than *P*-to-*s*, for WP1, some of the conversion

points at a depth of 70 km fall on the eastern side of Palau-Kyushu ridge that is different in age from western Philippine Sea (Figure 1). These two regions are divided by the Palau-Kyushu ridge roughly at the center of Philippine Sea plate. We stacked SRFs from WP1 into two groups based on the geographical locations of piercing points (Figure 5) in order to estimate LAB depths of two different geochronological regimes. In Figure 4a, function a1 shows the stacked radial-RF (PRF), while functions b1 and c1 are the stacked SRFs for western Philippine Sea basin and Parece-Vela basin, respectively. Figure 4b shows the stacked RFs for station WP2. In Figure 4, components a2, b2, and c2 are the corresponding *Z* component and *Sv* components (i.e., deconvolved by themselves) for WP1, and components d2 and e2 are for WP2.

[14] In order to estimate error in stacking, we employed the bootstrap technique [*Efron and Tibshirani, 1993*] to each set of data by resampling 500 times. Each time, we constructed a resampled observed data set (of an equal size to the observed data set) that was obtained by random sampling with replacement from the original data set, and then we stacked resampled seismograms after a moveout correction. Those 500 bootstrap stacked seismograms are then used to estimate the standard error (SE) of the final stacked trace.

[15] In Figure 6, we also plot the image for PRF in distance bins for both the stations. There are at least two prominent discontinuities present in the first 10 s of RFs (roughly corresponding to depths of 0 to 100 km beneath the station), one with positive polarity corresponding to the oceanic Moho, followed by a negative discontinuity, which we interpreted as the LAB. Crustal phases in both regions are observed at a delay time of ~ 1 s, corresponding to 7 to 8 km thick oceanic crusts that are close to the regionally determined estimates based on active seismic data [*Shinohara et al., 2008*] and to the global average [*White et al., 1992*].

3.2. Effects of Water Reverberations

[16] Since the seismic observatories are situated at a depth of ~ 500 m below the ocean floor and there is a ~ 5 km thick water column above, the seismic waveforms should be affected by water reverberations, generated mostly by *P* waves. To estimate their effect on both the RFs we first generated a suite of synthetic cases. Let us first see the schematic raypaths for the *P* and *S* waves and their converted waves as shown in Figure 7. In case of PRF, a substantial amount of water reverberations interfere mostly with the vertical component (Figure 7a) as *P* waves coming from a

Table 4. WP2 *S* Wave

Origin Time	Latitude (deg)	Longitude (deg)	Depth (km)	m_b
2000-10-31_18:43:20.890	-17.87	-175.31	33	5.4
2001-08-05_05:16:16.900	12.22	93.35	96.4	5.4
2001-08-21_06:52:06.199	-36.81	-179.57	33	6.4
2001-09-29_02:40:07.400	-18.5	168.16	33	5.5
2001-09-15_15:04:34.100	-22.39	-175.01	10	5.6
2001-11-05_23:07:11.700	-17.29	-179.25	564.1	5.4
2001-12-03_11:32:29.800	-16.5	-177.54	10	5.7
2002-01-02_17:22:48.800	-17.6	167.86	21	6.3
2002-04-18_05:02:46.190	16.99	-100.86	24.9	5.4
2002-06-22_02:58:21.290	35.63	49.05	10	6.2
2002-06-27_05:50:35.090	-6.96	104.18	11	6.0
2002-06-30_21:29:36.300	-22.2	179.25	620	5.5

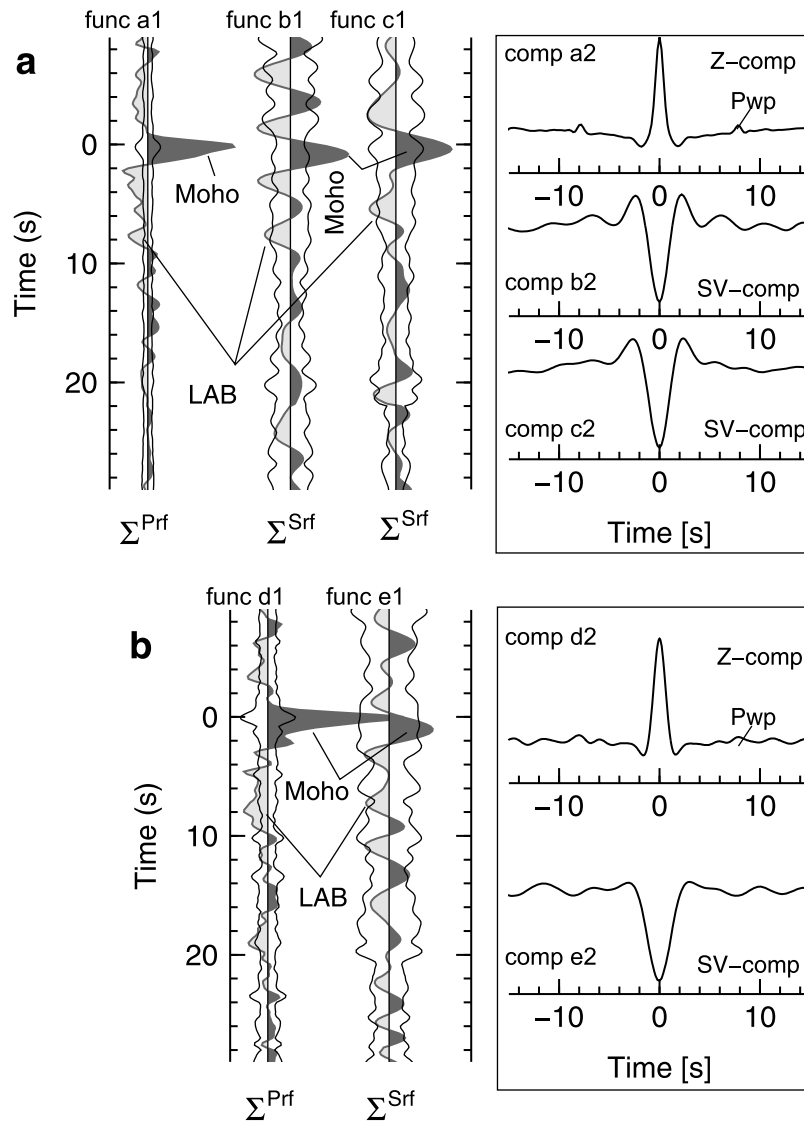


Figure 4. Stacked receiver functions (RFs) for the stations (a) WP1 and (b) WP2. In Figure 4a, function a1 is the radial PRF with its corresponding vertical component, a2; functions b1 and c1 are the S wave RFs (SRFs) for West Philippine (WP) basin and Parece-Vela (PV) basin data (see Figure 1 for the location of basins and Figure 5 for the distribution of conversion points in the Philippine Sea plate) with their corresponding S_v components, b2 and c2, respectively. For WP2 in Figure 4b, function d1 is radial PRF with its corresponding vertical component, d2, and function e1 is the SRF with its corresponding S_v component, e2. P_{wp} is the P wave reverberation coming from a thick water layer (in case of WP1 the water column is 5666 m and for WP2 it is 5710 m). Strong P wave water reverberations are only seen in the vertical component of the P wave RF (PRF), while the radial components are least affected. On the other hand, the SRFs are not contaminated by $P_{wp}(s)$ since these are later arrivals than primary S phases in the SRF (see Figure 8). The converted phases from the Moho and lithosphere-asthenosphere boundary (LAB) are labeled. Two bounding wiggles in each trace represent the error bounds of the stacked signals of two σ standard errors. The stacked traces were made after moveout correction with reference slowness of 6.4 s/deg using the IASP91 Earth model.

teleseismic distance propagate into the water column in near vertical paths owing to Snell's law. On the other hand in case of SRF, these water multiples also interfere with the vertical component, however its timing of arrival will be later than the primary S phase, thus making SRF uncontaminated in the time window of our interest. To minimize the water multiples in case of PRF analysis, we therefore prefer the radial receiver

functions for P -to- s conversions, whereas in case of SRF, we used the P - S_v coordinate.

[17] In order to estimate the P wave reverberations, their timing and amplitude through water layer, we generated a number of synthetics (Figure 8) with various plausible models, namely, crust + half-space, water + crust + half-space, and water + crust + LID + half-space. In the latter

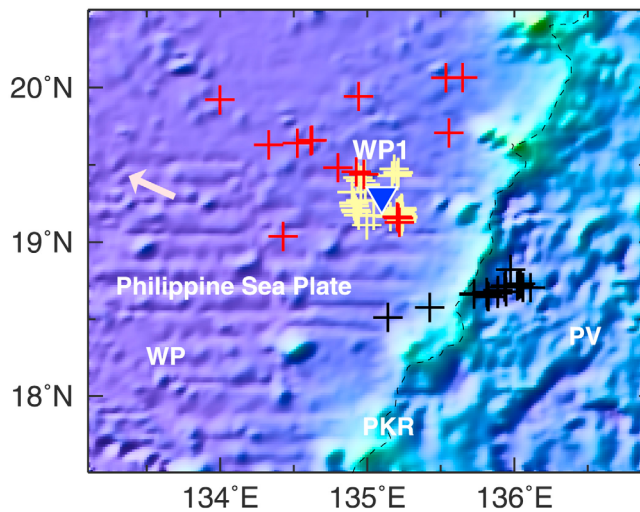


Figure 5. Topographic image of the Philippine Sea plate around the seismic station WP1 (inverted blue triangle). Palau Kyushu Ridge (PKR) runs almost in the center of the Philippine Sea plate from north to south and divides the plate into two distinct geological provinces: PV, Parece-Vela basin (15–27 Myr); WP, Western Philippine basin (33–49 Myr). Crosses in yellow and red are the piercing points for P to s and S to p converted waves, respectively, at 70 km depth falling in the WP, whereas crosses are the piercing points for S -to- P conversion falling mostly in the PV. Only S -to- P piercing points sample the PV owing to its larger slowness.

two cases we fixed the receiver depth below the hard surface so as to mimic the actual ground scenario. In Figure 8a, we have only the conversion from Moho and its multiples. The multiples are weak due to the gradient layering above the Moho [Shinohara *et al.*, 2008]. If we increased the gradient above Moho more, then its multiples would be lesser in amplitude (also discussed in detail in Figure 16). On the other hand in Figure 8b, we have crust and half-space but a water layer of 5 km thickness was introduced on top. Now, if we see the PRF, the Z component is severely affected by water multiples, namely P_{WP1} , P_{WP2} , and so on, but in the R component their amplitudes are much smaller compared to the Z component. In case of SRF, however, the main converted phases from Moho (Smp) and all other multiples are on the other side of the primary phase from each other. Finally, in case where we have two boundaries, Moho and LAB as shown in Figure 8c, the Z component of PRF is similar to the above case, but in the radial component there are phases from Moho, its multiples and a negative phase from LAB. As in this model the thickness of water layer and lithosphere is such that P_{WP} and Pls (conversion from LAB) are falling in similar times. In the SRF panel (Figure 8c), all the multiples and main phases are clearly separated in time, Smp and Slp are in one side and all the multiples are in another side of primary phase in time domain. This makes the SRF an effective tool to resolve the ambiguity.

3.3. Modeling of LAB

[18] The receiver function results for both the seafloor borehole broadband seismic stations show consistent positive and negative phases in time that we interpreted as Moho

and LAB signatures, respectively (Figure 4), and this observation will be further examined by the observations of backscattered LAB phases in the later sections. In order to construct representative structural models beneath WP1 and WP2, we modeled the stacked RFs. We used the reflectivity method for isotropic layers to calculate synthetic waveforms. The oceanic crustal model and upper mantle velocities were fixed to those derived from seismic reflection-refraction surveys [Shinohara *et al.*, 2008]. The water column thickness and receiver depths at the respective places are known fairly accurately. Although we observe in the previous section that presence of water column affects the PRF to some degree, the amplitude of the water multiple on the PRF appeared small to match with the observed amplitude of the negative phases around ~ 7 – 8 s in PRF. Hence it compelled us to introduce an additional low-velocity layer at the corresponding depths to match the observed amplitudes in PRFs as well as in the SRFs as presented in Figures 9–11.

[19] The green traces in Figures 9–11 are for the model without LAB. The small negative arrivals in the PRFs are due to the water multiples. To constrain the depths of the LABs we used the crustal and upper mantle velocity information as a priori inputs to our models, and only the depth and contrast at LABs are varied. In order to generate a reasonable structure matching with the observed data, we

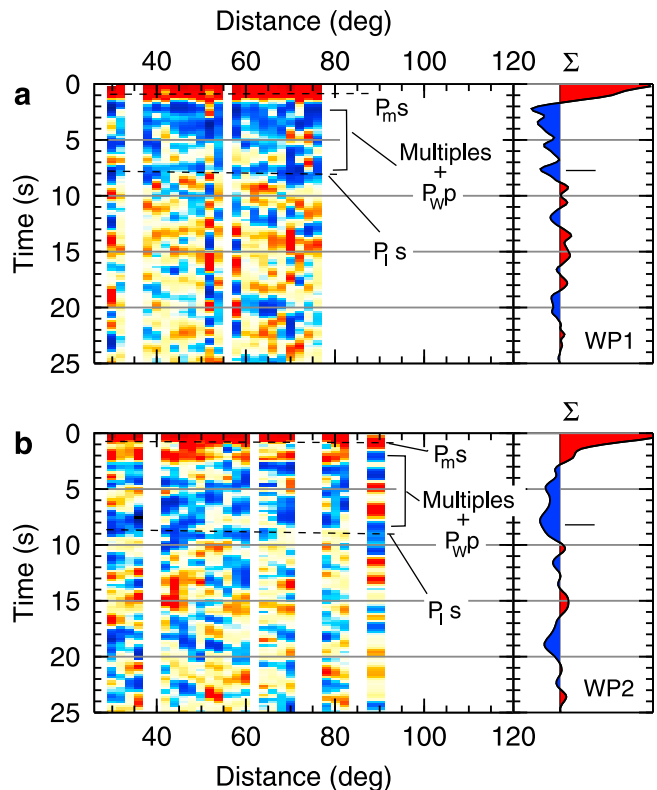


Figure 6. (left) Image of the radial PRFs for (a) WP1 and (b) WP2 plotted with increasing epicentral distance. The main converted phases, i.e., Pms , Pls , and water reverberations P_{WP} and crustal multiples are marked. (right) Stacked traces after moveout correction with respect to the IASP91 model with reference slowness of 6.4 s/deg. The horizontal lines in the sum trace indicate the negative phases coming from the LAB.

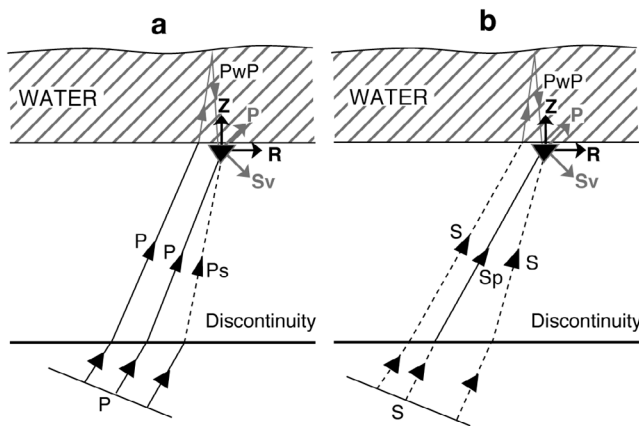


Figure 7. Schematic ray diagram showing raypaths for (a) P_s and (b) S_p conversions from a discontinuity below the station (inverted triangle). There is a thick water layer column above the station. Z and R are the vertical and radial directions, respectively. It is clear that the P wave traveling in the low-velocity water medium travels almost vertically and is reflected back from the water surface to interfere with the Z component, while the orthogonal R component remains least contaminated. P and S_v are the local ray coordinate system, where P is along the direction of incoming primary wave.

employed a grid search scheme where the depth and the change in velocity (V_s) across the LAB were varied over a wide range of values. All the attempted LAB depths and changes in V_s are shown in Figures 9c, 10b, and 11c with shading. For every model a pair of RFs were computed (PRF and SRF) and each time we estimated the root mean square errors with respect to the observed waveform for the first 10 s of time window. To achieve a single velocity model which satisfies both the independent RFs, we used the weighted RMS (wrms) error giving weights to the estimated RMS of PRF and SRF separately and then normalizing. The values of weight for the respective RFs were decided based on the error estimated for the stacked RFs using bootstrap (solid lines shown just near the label LAB in Figures 9–11). Here we defined the ratio of weights for each RF as the reciprocal of the ratio of standard errors at the peak time of the phases, since lesser error implies greater weight and more confidence in that trace. Finally, the optimal parameters were determined for the minimum wrms error contoured with depth versus V_s and that was taken as our preferred model (shown in Figures 9d, 10c, and 11d). For WP1, the weights for PRF and SRF are 0.6 and 0.4 to get the wrms error, respectively, whereas in case for WP2 the weights for PRF and SRF are 0.7 and 0.3, respectively.

[20] As mentioned earlier, the station WP1 in the central Philippine Sea is located near the Palau Kyushu Ridge (PKR), and observed SRFs are grouped into two depending on the location relative to PKR of the piercing points of the LAB signals (Figure 5). The prominent phases corresponding to LAB occur at ~ 7.5 s (76 ± 1.8 km, 1 SE) for both PRF and SRF for piercing points located directly beneath the station, which is situated in the west of PKR with a plate age of ~ 49 Myr. The same LAB phase was observed ~ 2 s earlier (~ 55 km LAB) for SRF of eastern piercing points where

the plate age is ~ 25 Myr. For WP2 in the northwestern Pacific Ocean where the plate age is ~ 129 Myr, the data quality was lower, but we still observed similar LAB phases at ~ 7 – 8 s for both PRF and SRF. The waveform modeling gave the best estimate for LAB depth of 82 ± 4.4 km. The drop in V_s was found to be large in both the stations to be ~ 7 – 8 (± 0.84) %.

4. Stacking Analysis Without Deconvolution

[21] In the presence of strong water multiples, the deconvolution procedure inherent in the conventional receiver function technique may introduce spurious phases that might be interpreted as a real phase. In fact, the time domain deconvolution method (provided in SeismicHandler version 5.0a, based on *Berkhout* [1977]) used by *Kawakatsu et al.* [2009a] tends to underestimate, compared to other methods such as the spectral division, the effect of the water multiples on radial PRFs when applied to noise free synthetic waveforms; however, results of different deconvolution techniques are similar when applied to noisy synthetic waveforms whose S/N ratios are comparable to that in the real data, and thus the effect is unlikely to be important (reverberation phases are affected more by noise because of their periodicity that results in spectral notches in the absence noise). Nevertheless in this section, we attempt to extract structural signals directly from waveforms without deconvolution to avoid the potential problem. Also the vertical component used for the deconvolution in the RF method itself contains valuable information to constrain the subsurface structure at the station. In order to utilize the maximum of the information in the data, we further conduct stacking analyses without deconvolution.

4.1. Reflected Phases in Vertical Components

[22] In the recent efforts using Green's function at the receiver site, it was possible to extract the reflected P phases [*Kumar and Bostock*, 2008; *Langston and Hammer*, 2001]. The P wave backscattered phases are registered in the vertical components of the waveforms. We look into our data for reflected as well as converted phases in vertical and radial components, respectively, using a plain summation technique without using the deconvolution which is used in receiver function techniques as described earlier. The approach is similar to the technique used by *Shearer* [1991] who used it for long-period seismograms. Recently, *Kumar et al.* [2010] used a similar technique on broadband data for permanent stations and showed that the results were consistent with the receiver function results, and in addition they observed reflected phases in vertical components. However, the signal-to-noise ratio was lesser than that obtained using deconvolution.

[23] The observation of backscattered phases provides additional constraint on subsurface seismic parameters. Here we used the same approach to the data from WP1 and WP2. The steps used for analysis are simple and can be summarized as follow: first, all raw waveforms are rotated into the radial and transverse components using theoretical back azimuths. Then the maximum amplitude (the sign is reversed if the absolute value of the minimum is larger than the maximum) in the P wave group on the Z component of each trace is normalized to one, and all traces are lined up along this maximum P amplitude. This is the same procedure as in

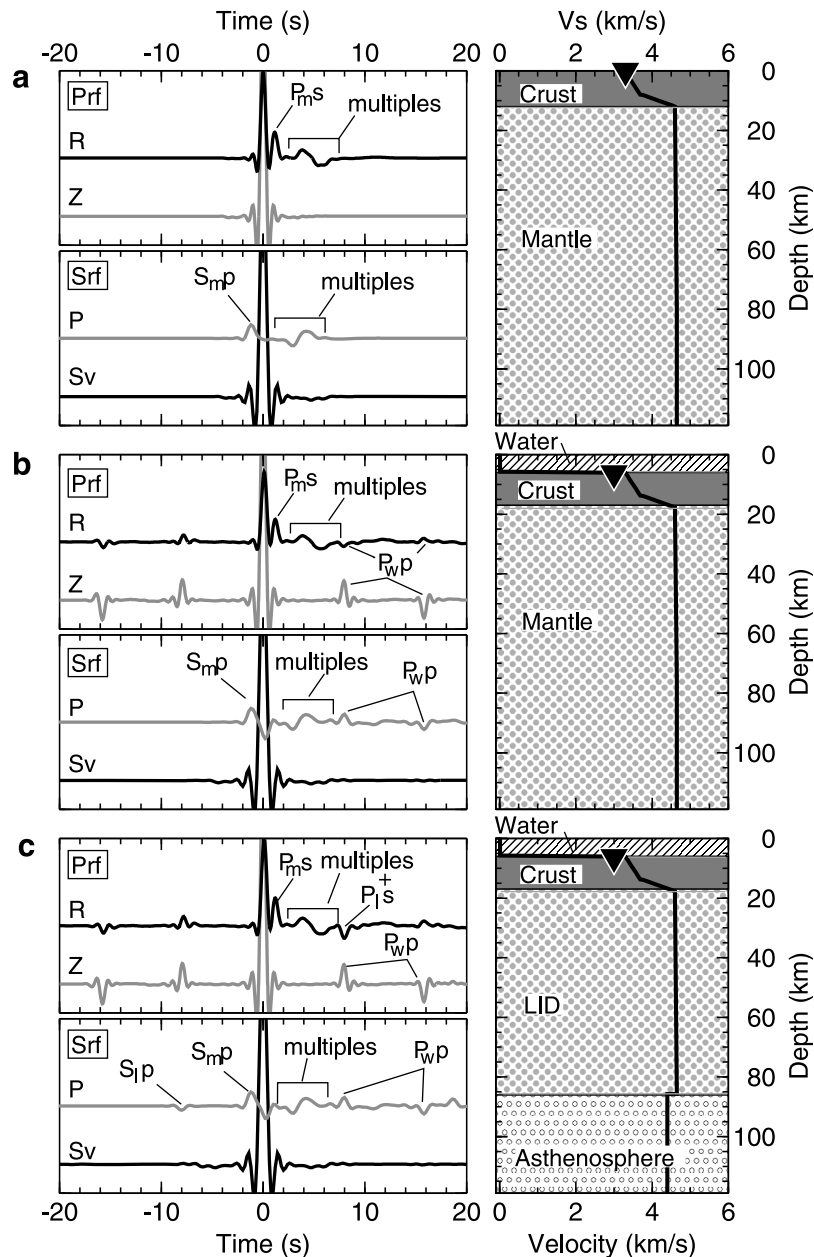


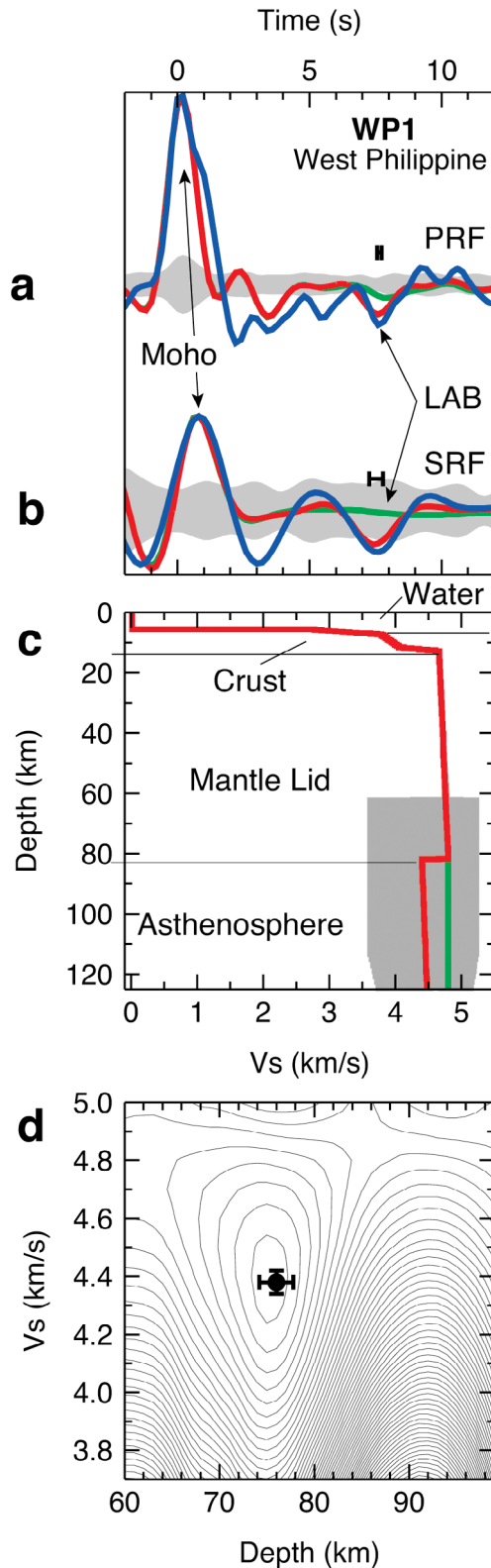
Figure 8. (a–c) Synthetic P and S receiver functions to show the effect of water reverberations on the various forward and backscattered phases. (top) PRFs and (bottom) SRFs with their two components, namely, P/Z in shading and R/Sv components in wiggles, respectively. (right) Model used for the respective synthetics. The synthetic code can take into account the station depth within the seafloor (similar to the observed scenario). In Figure 8a, the model contains only a gradient in the crust followed by a half-space, and the receiver is located on the free surface. Figure 8b shows the case for which we have a 6 km water column above, and the receiver is at 500 m below the seafloor, whereas in Figure 8c, the model is the same as Figure 8b, but we have a negative discontinuity at 85 km depth. The phases that occur at negative time in the synthetic PRFs in Figures 8b and 8c are artifacts of deconvolution due to water layer reverberations and have no physical meaning.

the deconvolution technique except that in the latter case P waveforms are simpler and more similar, i.e., more spike like. The next step before summation is the moveout correction that is required to correct for the distance dependence of the differential times of P and the reflected/converted phases. The IASP91 model [Kennett and Engdahl, 1991] with a reference

slowness of 6.4 s/degree [Yuan *et al.*, 1997] was employed for the correction. For converted and reflected phases, we use respective moveout corrections separately.

[24] Figure 12 shows the synthetic vertical component in case of a thick water column and borehole receiver with crust and LAB. The synthetics have been generated using

the reflectivity method. Figure 12a shows a schematic ray diagram for backscatters. The synthetic vertical components are shown in Figure 12b corresponding to the model in Figure 12c (to show the phases clearly, we use a somewhat large drop in V_p at LAB of 4.3%). It is clear that the second



water multiple is negative in polarity whereas the LAB reflected phase P_{LP} is positive, and all other water reverberations are with alternate polarities. The arrival times for these reflected phases depend on the velocity distribution and thicknesses of the water column and the lithosphere. In case for WP1, these two phases come very close (Figure 13a) and make an ambiguous scenario. However, for WP1 we may still see a coherent positive P_{LP} (Figure 13a) despite the negative P_{wp2} close to it. For WP1, the first negative phase (blue dashed line) is P_{MP} , the Moho reflected phase, and at around ~ 8 s, ~ 16 s and so on are P_{wp1} , P_{wp2} , \dots , with alternate polarities. Juxtaposing with P_{wp2} (negative) at slightly more than 18 s there is a positive phase that may originate from LAB (P_{LP} , marked 3 in Figure 13a, bottom).

[25] On the other hand, in the case of WP2 (Figure 13b) beneath which the LAB depth is estimated to be deeper than for WP1, the same P_{LP} (marked 3 in Figure 13b, bottom) and P_{wp2} appear well separated. The P_{MP} is observed at WP2, but the first water multiple, P_{wp1} (positive), is not very clear, possibly due to the location of the seismic station within the borehole (the borehole depth for WP2 is ~ 100 m more than WP1). The second water multiple P_{wp2} (-) and P_{LP} (+) are well visible at ~ 16 s and ~ 20 s. In both the stations the reflected phases from Moho, P_{MP} and from LAB, P_{LP} are seen at least in individual bin data, although in WP1 the water multiple and P_{LP} are intermittently seen in the slowness plot (Figure 13, top). However, in the summation plots shown in Figure 13 (bottom), without moveout (amplitudes a1 and b1) and with moveout for reflected phases (amplitudes a2 and b2), a small positive phase is visible at 17–18 s for WP1 and ~ 20 s for WP2 that may be interpreted as P_{LP} .

4.2. Converted Phases in Radial Components

[26] Figure 14 shows the stack of radial components by plain summation, i.e., without deconvolution. Here we show stacked traces both with and without moveout correction. Again in the radial components of seismograms we observe at least two phases beyond the error bounds of 2 standard errors (SEs) in all of the traces. The first at 0–1 s is positive (Moho) and ~ 7 –8 s is a negative (LAB). The negative phases marked as Pls are the converted phases at LAB, and are well in the agreement in times with the receiver functions shown in Figure 4. This negative phase confirms the existence of LAB, and is not a water reverberation, as water

Figure 9. Modeling results for WP1 in the Western Philippine basin. (a, b) Blue color traces are the observed PRF and SRF, and red traces are the synthetic for (c) the model. The green trace is the synthetic for a model without LAB, as shown in Figure 9c. Small horizontal bars near label LAB are the bootstrap error estimates (1 standard error) of the peaks of LAB time. To constrain the lithospheric depth and relative percentage V_s drop across the LAB, we employed a grid search technique (d) fixing the crustal and upper mantle parameters from reflection–refraction seismic experiments [Shinohara et al., 2008]. The error bars in the center of the contour give the uncertainties (1 standard error) in depth and δV_s based on the bootstrap estimates. The standard errors (2 times SEs) of the stacked traces shown in Figures 9a and 9b by shading are also given in Figure 4.

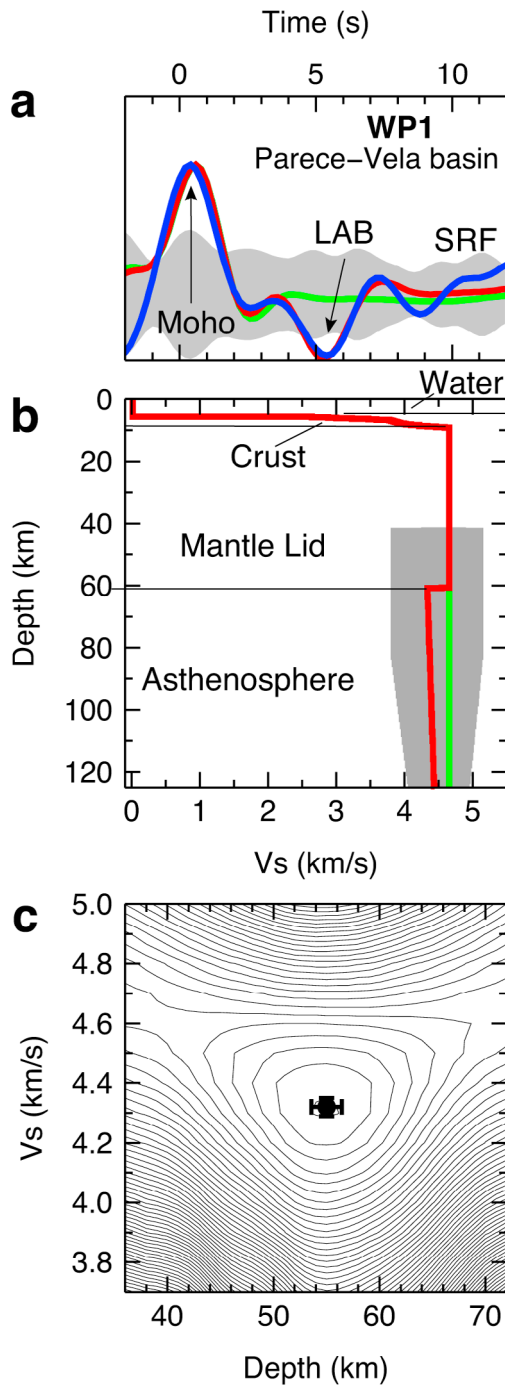


Figure 10. Modeling results for WP1 in the Parece-Vela basin. Same as Figure 9, but for SRF, whose conversion points are falling in the eastern side of PKR, i.e., the lithospheric estimate is for the Parece-Vela basin (PV).

reverberations in the radial component around these times will be of positive polarity. Note that in the case of WP1 there is appreciable energy in the acausal ($t < 0$ s) part of the seismogram caused by the negative swing of the main P pulse, as the stack is centered on the timing of the maximum of the P wave train. As deconvolution is not involved here, this acausal side lobe has no influence on the causal part.

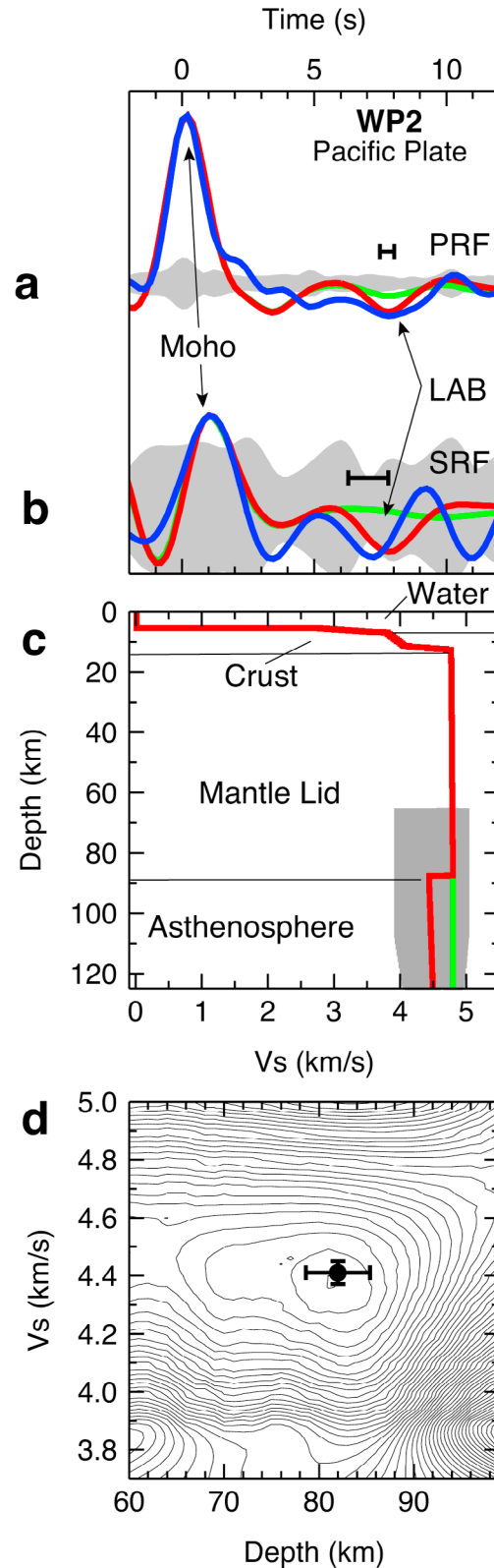


Figure 11. (a–d) Modeling results for WP2. Same as Figure 9, but for WP2, situated in the northwest Pacific ocean. The stack trace at Figure 11a has been plotted with a low-pass filter with corner frequency of 0.5 Hz.

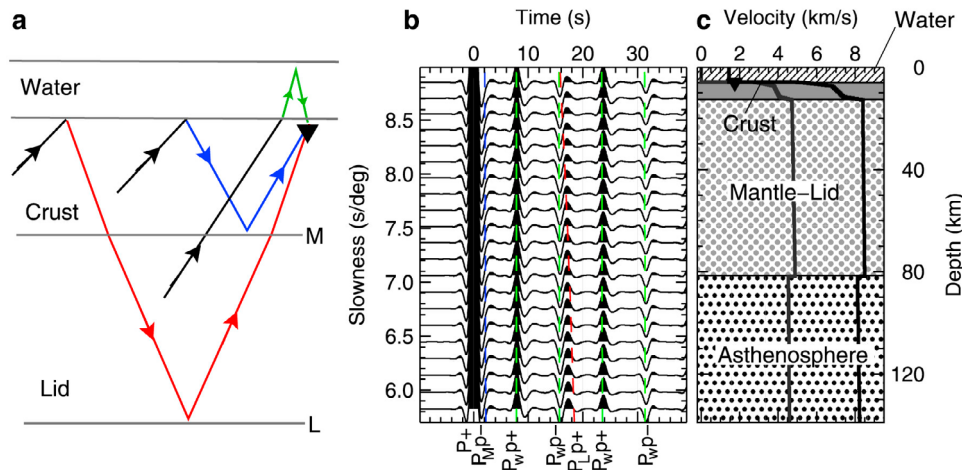


Figure 12. (a) Schematic raypaths for various reflected phases. (b) Synthetic vertical component of seismograms derived in a similar way as described in the text for (c) the model. The seismograms are not a deconvolution result, as in receiver functions, but the plain vertical component with corresponding P waves normalized. Figures 12a–12c clearly show the presence of different reflected phases (in different colors) with different polarities that can be compared with Figure 13.

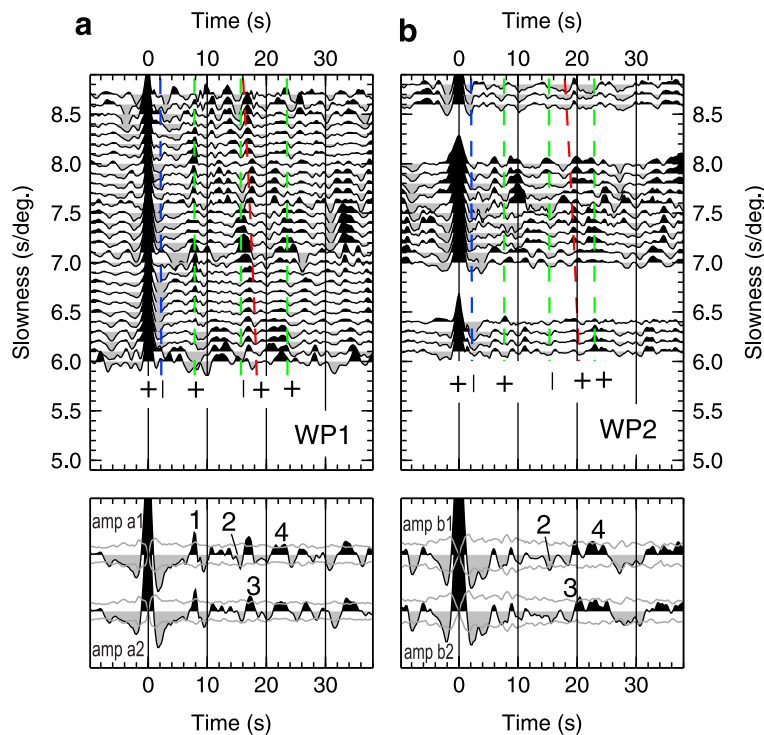


Figure 13. (top) Observed vertical component of seismograms derived without deconvolution for station (a) WP1 and (b) WP2 plotted with increasing slowness. P to p multiply reflected phases from the Moho (P_{MP}), LAB (P_{LP}), and water reverberations are visible with relevant polarities. The plots are made at a bin spacing of slowness 0.1 s/deg with an overlapping window of 0.2 s/deg. Dashed lines are approximate travel times for the respective models for the WP1 and WP2. Blue is P_{MP} (reflection from Moho, negative polarity), green is P_{WPs} (water reverberations, positive, negative, positive, . . . polarities, respectively), and red is P_{LP} (reflection from LAB, positive polarity). (bottom) Stacked traces for the respective stations without moveout corrections (amplitudes a1 and b1). The traces in amplitudes a2 and b2 are stacked with moveout corrections for reflected phases with reference slowness of 6.4 s/deg using IASP91 model. The numbers 1, 2, 4 are the water multiples, while 3 is the reflected phase from LAB. Two bounding lines at both side of the traces are the 2σ standard error.

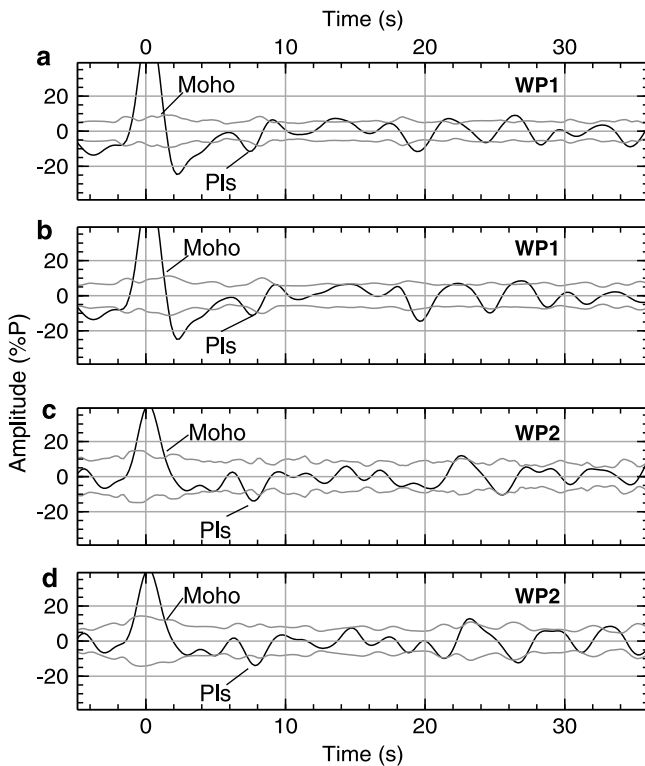


Figure 14. The stacked radial component seismograms derived from plain summation without deconvolution for the stations WP1 and WP2, similar to Figure 13, but for the radial component. (a, b) Moveout corrected for P_s and plain stack, respectively, for the station WP1. (c, d) Moveout corrected and plain stack, respectively, for the station WP2. The main phases are marked. The results match well with the receiver function computed using deconvolution in Figure 4. The shaded lines on both sides of the mean lines are the standard error estimated using bootstrap for $\pm 2\sigma$. A detailed discussion is given in the text.

[27] Figure 15 depicts the vertical and radial components of raw synthetic seismograms corresponding to the plain summation case for various models. Figure 15a is the case where we have only a water column and a half-space. In the vertical component we have larger amplitudes of water reverberations, but in the radial there are projected water reverberations with much smaller amplitude and with positive polarity in a similar time. In Figure 15b, we introduce a gradient crust, and so we have, in the radial component, crustal multiples within 4 s and smaller amplitude subsequent multiples. In the case of Figure 15c where we have water + crust + LID + half-space, the vertical component contains water reverberations and one additional positive phase near 17 s coming from the downgoing P wave (P_{lp}). The negative phase can also be seen in radial component with appreciable energy at ~ 7 s (Pls) arising from a conversion from the LAB.

[28] In order to show that the negative phases observed in Figure 14 are not from crustal multiples, we further compare synthetics with gradient [Shinohara *et al.*, 2008] and sharp crustal models with water on top. Figures 16a and 16b show the raw synthetic (i.e., without deconvolution) vertical and radial components for the models shown in Figure 16c. If

we compare the vertical components of synthetics, the water reverberations P_{wp} are registered in them. The radial components show that the amplitudes of crustal multiples (less than 5 s) and subsequent multiples are smaller in case of a gradient at the base of the crust (Figure 16b) than that for the sharp crust (Figure 16a). However, even in the sharp case the amplitudes of multiples are much smaller than that of the negative LAB signal. For comparison, we overlay the radial component of the observed stacked traces (from Figure 14) from WP1 as a shaded line. The negative phase as observed at ~ 7 –8 s in our observed traces cannot be reconciled by the crustal effect as seen in the radial synthetics, as the multiples are of much smaller and positive amplitudes.

5. Discussion

5.1. Azimuthal Seismic Anisotropy

[29] The active source experiments [e.g., Hess, 1964; Raitt *et al.*, 1969; Asada and Shimamura, 1979; Shearer and Orcutt, 1986; Shinohara *et al.*, 2008] indicate the existence of azimuthal seismic anisotropy in the oceanic lithosphere. For example, Shinohara *et al.* [2008] conducted an active source survey for the structure around WP2, and from the observation of P_n and S_n arrivals, they revealed an azimuthal

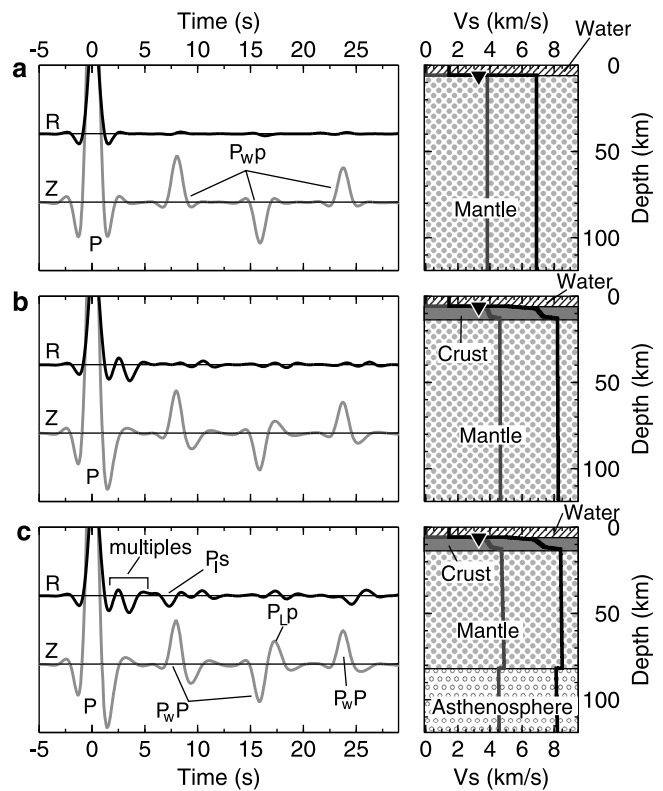


Figure 15. (left) Synthetic vertical and radial component seismograms without deconvolution for (right) the different models. The radial components are normalized with respect to their corresponding P waves in the vertical components. (a) A model with only water at the top and the station ~ 500 m below the seafloor. (b) Only water and crust. (c) Water, crust, and LAB. Synthetics are calculated for a reference slowness of 6.4 s/deg.

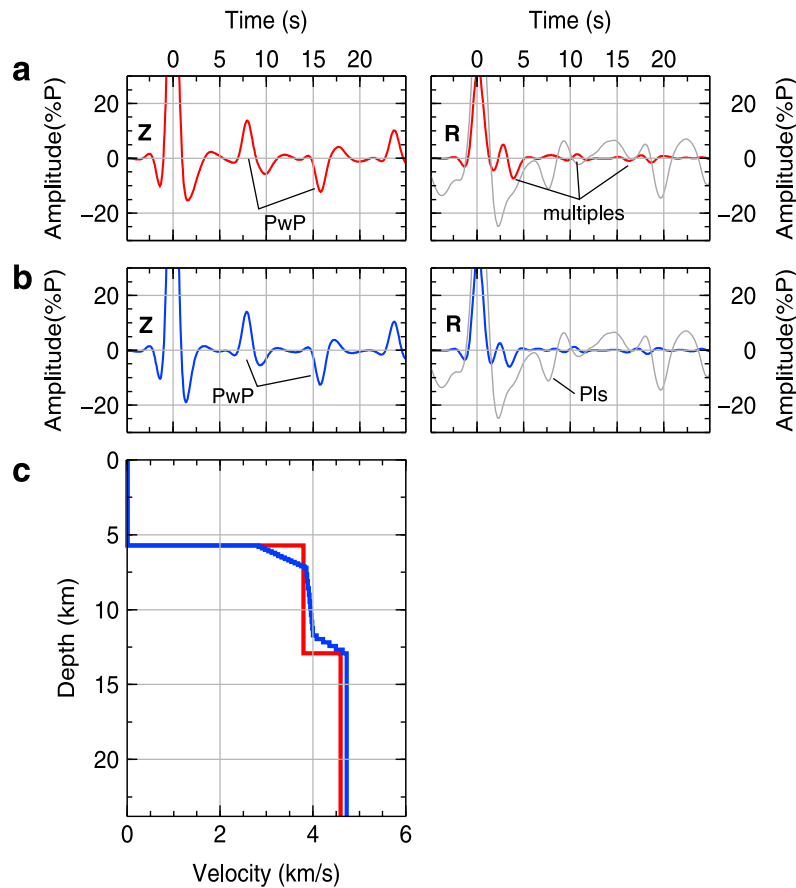


Figure 16. (a, b) Synthetic vertical and radial seismograms for (c) the models. All the traces are scaled by taking their corresponding *P* wave as unity. The color of the seismograms corresponds to the color of the models shown in Figure 16c, i.e., red color model is with a sharp Moho, while blue is a model having a gradient just above the Moho. (left) Vertical components. (right) Radial components. In Figure 16 (right), the shaded trace is the observed stacked radial component without deconvolution shown in Figure 14. The model contains a water column of thickness ~ 6 km at the top. Synthetics are calculated for a reference slowness of 6.4 s/deg.

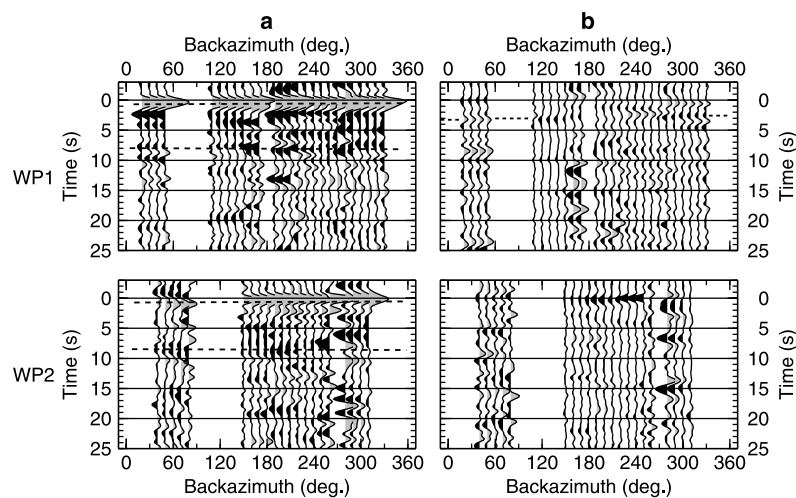


Figure 17. The observed receiver functions for the stations WP1 and WP2 plotted with increasing back azimuth of the events. (a) Radial and (b) transverse component of the receiver functions. The plots are generated using bins at 10° spacing with an overlapping window of 15° half-width in back azimuth. In Figure 17a, there are two prominent phases marked by dashed lines. In Figure 17b, no such corresponding prominent amplitudes are visible, except at ~ 3 s, where a signature of layering within the lithosphere may be present.

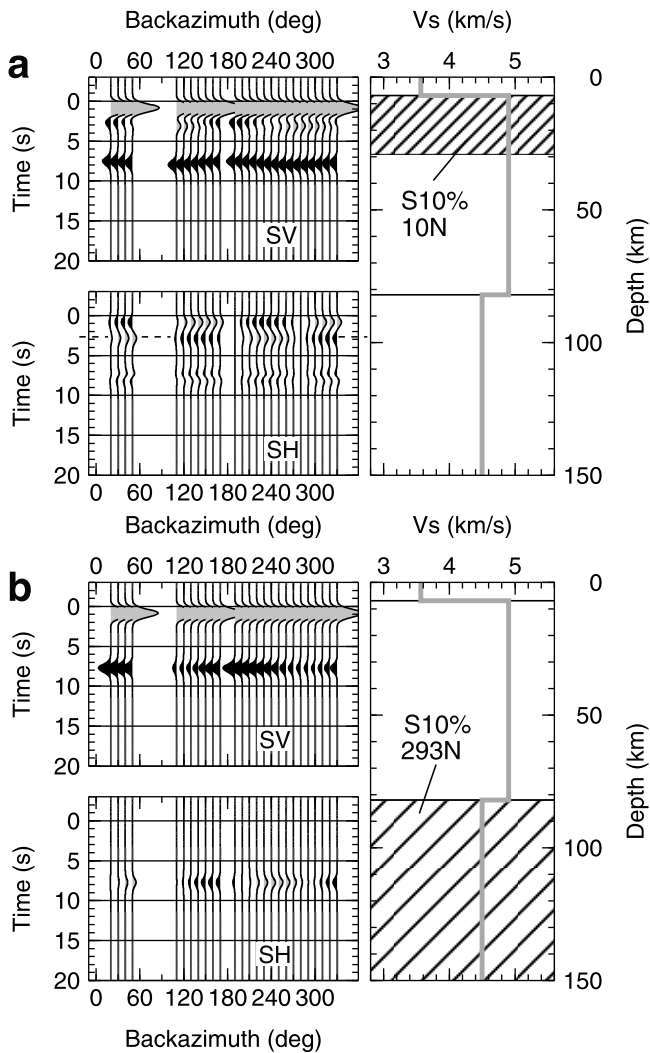


Figure 18. (left) Synthetic SV (radial) and SH (transverse) component P receiver functions for (right) the model. (a) A possible model to explain the polarity reversal with back azimuths observed in Figure 17b at ~ 3 – 4 s for WP1. We introduce an anisotropic layer of thickness 27 km in the uppermost mantle with anisotropy in V_s of $\pm 5\%$ and the fast polarization axis along 10°N . (b) A model where the whole lithosphere is isotropic but the asthenosphere is anisotropic ($\pm 5\%$ in V_s), with a fast direction along the plate motion direction of 293°N (nearly common at both stations).

anisotropy ($\pm 2.7\%$ in V_p and $\pm 2.1\%$ in V_s) for the sub-crustal lithospheric mantle with a fast direction nearly perpendicular to the ancient spreading direction (310°N). Thus the effect of the azimuthal anisotropy on our data set deserves investigation.

[30] Figure 17 shows the radial and transverse components of PRF. For both WP1 and WP2, we do not observe any appreciable energy in the transverse components (Figure 17b) except for WP1 at around 2–3 s where an indication of 90° azimuthal polarity reversal appears. This may represent a layering within the lithosphere at ~ 30 km depth as suggested by *Shinohara et al.* [2008] for WP2. In order to estimate the

approximate anisotropic parameters we generate synthetics using a simple plane layer model [*Frederiksen and Bostock, 2000*] with sharp Moho and LAB at 7 and 82 km, respectively (without water layer). After many trials, a model that might resemble the data is shown in Figure 18a. Here we place the anisotropic layer of thickness 27 km in the uppermost mantle with anisotropy in V_s of 10% (i.e., $\pm 5\%$) and a fast polarization axis along 10°N that is not so different from the ancient spreading direction of the region ($\sim 30^\circ\text{N}$). Although we do not further investigate the effect of the azimuthal anisotropy in the present paper because of the absence of obvious energy in transverse components (Figure 17b), more systematic treatment including SKS splitting may be desired. For reference, another model where the whole lithosphere is isotropic and the asthenosphere is anisotropic ($\pm 5\%$ in V_s) with a fast direction along the plate motion direction of 293°N (nearly common at both stations) is shown (Figure 18b). In this case, energy on the transverse component is visible at ~ 7 – 8 s, and on the radial component, the amplitude of the negative LAB phase at ~ 7 – 8 s varies considerably.

5.2. LAB Beneath Normal Ocean

[31] The results of this paper suggest an apparent age dependence of the LAB depth beneath the normal oceanic area [*Kawakatsu et al., 2009a*]. It is based on, however, only three points of observation from the two stations, and thus it may be regarded as premature to discuss the origin of the oceanic LAB. Considering that some models of the LAB predict an age independent LAB depth of ~ 60 km [e.g., *Karato and Jung, 1998*], further independent analyses are warranted. The recent analysis of ScS reverberations in the northwest Pacific region along two different paths between Hawaii and the Japan-Izu-Bonin-Mariana arcs reports G discontinuities at depths of 83–89 km with an impedance reduction of $\sim 10\%$ [*Bagley et al., 2009*]. Considering that the bounce points of ScS reverberation phases at the surface of this study are concentrated in the old part of the northwest Pacific ocean, the result may be better representative of the LAB in old ocean than the earlier estimates of *Revenaugh and Jordan* [1991b]. The estimated depth and strength of the LAB appear comparable to our result for WP2 in the old ocean. We also note that *Kumar and Kawakatsu* [2011] recently showed an age dependence of the LAB of the oceanic plate around the rim of the northern Pacific Ocean.

5.3. Physical Nature of the Asthenosphere and a LAB Above

[32] Since our seismic observations are at a higher frequency of 0.25 Hz for PRF, the gradient in the LAB is likely to be less than ~ 15 km [e.g., *Bostock, 1999*; *Rychert et al., 2007*]. On the basis of a part of the analyses presented here (Figures 4 and 9–11) that reveal the presence of such a sharp LAB with a large velocity reduction ($\sim 7\%$ – 8% in V_s), *Kawakatsu et al.* [2009a] proposed a model of partially molten asthenosphere consisting of horizontal melt-rich layers embedded in meltless mantle beneath oceanic regions. This model was originally developed to explain the observed strong seismic LAB signals with a small amount of melt presence, as such a layered structure effectively reduces vertically propagating shear wave velocities [*Backus, 1962*].

This model is also capable of explaining the strong radial seismic anisotropy of the low-velocity zone observed beneath the ocean [e.g., *Tan and HelMBERGER, 2007; Nettles and Dziewonski, 2008*]. A simple analysis of this model indicates that the behavior of the LAB is quite different for propagation of teleseismic P and S waves; the velocity reduction for P is much smaller than that of S_v (about 1/3 (1/2) for an incident angle of 20° (25°)) [*Kawakatsu et al., 2009b*] an effect that should be testable by seismological means.

[33] Although it is highly speculative to use amplitudes estimated from stacks of seismograms without source equalization (i.e., deconvolution) unless the number of seismograms is very large [see *Kumar et al., 2010*], the observed amplitudes of P_{LP} in Figure 13 (amplitudes a2 and b2) (section 4.1) are ~10% of the primary P phase for WP1 and WP2. These values, if taken at face value, require a very large reduction of V_p at the LAB, larger than that of V_s . This suggests either (1) the aforementioned model needs modification, (2) the suggested observation of P_{LP} is in error, or (3) measured amplitudes are highly overestimated due to the absence of an adequate source equalization procedure and/or to the presence of large noise.

6. Conclusion

[34] The crustal and lithospheric structure of the normal oceanic plates are investigated using P and S receiver function analysis on the data from two seafloor borehole broadband seismic stations located in the central Philippine Sea and the northwest Pacific ocean. We particularly focus on the structure of the seismic LAB or G discontinuity, a seismically observed abrupt velocity reduction in the uppermost mantle that may define the top of the low-velocity layer. The depth of LAB (measured from the ocean bottom) for the Pacific plate under WP2 (~129 Myr) is estimated to be ~82 km, while that for Philippine Sea plate under WP1 (~49 Myr) is ~76 km. Further, the LAB depth for the eastern part of Palau-Kyushu ridge in the Philippine Sea plate (Parece-Vela basin, ~25 Myr) is estimated to be ~55 km. These LAB depth estimates suggest a thermally controlled origin for the oceanic LAB [*Kawakatsu et al., 2009a; Kumar and Kawakatsu, 2011*]. The waveform modeling result suggests that the V_s drop across the LAB is large ~7%–8% and may require the presence of partial melt beneath the LAB as advocated by *Kawakatsu et al. [2009a]*.

[35] The effects of a thick water layer above an oceanic seismic station (or OBS) are investigated using various synthetic models. A thick water column atop the seismic station interferes substantially with the PRF. The radial component of the PRF is less affected than the vertical one. The SRF is also not much interfered with by the water reverberations.

[36] To supplement the conventional receiver function analyses, we analyze the vertical and radial components of observed seismograms without deconvolution (i.e., plain summation [*Kumar et al., 2010*]). We observe converted and reflected phases, some of which are originated from the LAB, in radial and vertical components of P wave coda, respectively. The radial component of plain summation seismograms show prominent Pls with a negative polarity, supporting for the LAB as observed. The vertical components of plain summation seismograms show a phase with a positive polarity that may correspond to P_{LP} reflected from the LAB.

[37] **Acknowledgments.** The Ocean Hemisphere network Project is funded by the Ministry of Education, Culture, Science, and Technology of Japan. The Ocean Drilling Project also contributed to the station deployment. We thank the editor, Robert Nowack, and two anonymous reviewers for their meticulous comments. The associate editor of the *Journal of Geophysical Research—Solid Earth* is thanked for improving the grammar and flow of the manuscript. P.K. is supported by the JSPS fellowship provided by the Japan Society for the Promotion of Science, and this work is partly supported by Grant-in-Aid for Scientific Research 22000003 through JSPS. P.K. is grateful to the director of NGRI for granting him leave. Analysis has been done in SeismicHandler (K. Stammler), and figures were produced using GMT [*Wessel and Smith, 1995*].

References

- Anderson, D. L. (1995), Lithosphere, asthenosphere, and perisphere, *Rev. Geophys.*, *33*, 125–149, doi:10.1029/94RG02785.
- Anderson, D. L., and C. Sammis (1970), Partial melting in the upper mantle, *Rev. Geophys.*, *33*, 125–149, doi:10.1016/0031-9201(70)90042-7.
- Ando, M., Y. Ishikawa, and F. Yamazaki (1983), Shear wave polarization anisotropy in the upper mantle beneath Honshu, Japan, *J. Geophys. Res.*, *88*, 5850–5864, doi:10.1029/JB088iB07p05850.
- Angus, D. A., D. C. Wilson, E. Sandvol, and J. Ni (2006), Lithospheric structure of the Arabian and Eurasian collision zone in eastern Turkey from S -wave receiver functions, *Geophys. J. Int.*, *166*, 1335–1346, doi:10.1111/j.1365-246X.2006.03070.x.
- Araki, E., M. Shinohara, I. S. Sacks, A. Linde, T. Kanazawa, H. Shiobara, H. Mikada, and K. Suyehiro (2004), Improvement of seismic observation in the ocean by use of seafloor borehole, *Bull. Seismol. Soc. Am.*, *94*, 678–690, doi:10.1785/0120020088.
- Asada, T., and H. Shimamura (1979), Long range refraction experiments in deep ocean, *Tectonophysics*, *56*, 67–82.
- Backus, G. E. (1962), Long-wave elastic anisotropy produced by horizontal layering, *J. Geophys. Res.*, *67*, 4427–4440, doi:10.1029/JZ067i011p04427.
- Bagley, B., A. M. Courtier, and J. Revenaugh (2009), Melting in the deep upper mantle oceanward of the Honshu slab, *Phys. Earth Planet. Inter.*, *175*, 137–144, doi:10.1016/j.pepi.2009.03.007.
- Berkhout, A. J. (1977), Least square inverse filtering and wavelet decomposition, *Geophysics*, *42*, 1369–1383.
- Bostock, M. G. (1999), Seismic waves converted from velocity gradient anomalies in the Earth's upper mantle, *Geophys. J. Int.*, *138*, 747–756, doi:10.1046/j.1365-246x.1999.00902.x.
- Burdick, L. J., and C. A. Langston (1977), Modeling crustal structure through the use of converted phases in teleseismic body-wave forms, *Bull. Seismol. Soc. Am.*, *67*, 677–691.
- Deuss, A., and J. H. Woodhouse (2002), A systematic search for mantle discontinuities using SS-precursors, *Geophys. Res. Lett.*, *29*(8), 1249, doi:10.1029/2002GL014768.
- Efron, B., and R. Tibshirani (1993), *An Introduction to the Bootstrap*, Chapman and Hall/CRC, Boca Raton, Fla.
- Ekström, G., and A. M. Dziewonski (1998), The unique anisotropy of the Pacific upper mantle, *Nature*, *394*, 168–172, doi:10.1038/28148.
- Farra, V., and L. Vinnik (2000), Upper mantle stratification by P and S receiver functions, *Geophys. J. Int.*, *141*, 699–712, doi:10.1046/j.1365-246x.2000.00118.x.
- Faul, U. H., and I. Jackson (2005), The seismological signature of temperature and grain size variations in the upper mantle, *Earth Planet. Sci. Lett.*, *234*, 119–134, doi:10.1016/j.epsl.2005.02.008.
- Forsyth, D. W. (1975), The early structural evolution and anisotropy of the oceanic upper mantle, *Geophys. J. R. Astron. Soc.*, *43*, 103–162.
- Frederiksen, A. W., and M. G. Bostock (2000), Modelling teleseismic waves in dipping anisotropic structures, *Geophys. J. Int.*, *141*, 401–412, doi:10.1046/j.1365-246x.2000.00090.x.
- Fukao, Y., et al. (2001), The Ocean Hemisphere network Project (OHP), in *Workshop Report of OHP/ION Joint Symposium, Long-Term Observations in the Oceans*, pp. 13–29, Earthquake Res. Inst., Univ. of Tokyo, Tokyo.
- Gu, Y. J., A. M. Dziewonski, and G. Ekström (2001), Preferential detection of the Lehmann discontinuity beneath continents, *Geophys. Res. Lett.*, *28*, 4655–4658, doi:10.1029/2001GL013679.
- Gutenberg, B. (1959), *Physics of the Earth's Interior*, 240 pp., Elsevier, New York.
- Hess, H. H. (1964), Seismic anisotropy of the uppermost mantle under oceans, *Nature*, *203*, 629–631, doi:10.1038/203629a0.
- Hirth, G., and D. L. Kohlstedt (1996), Water in the oceanic upper mantle: Implications for rheology, melt extraction and the evolution of the lithosphere, *Earth Planet. Sci. Lett.*, *144*, 93–108, doi:10.1016/0012-821X(96)00154-9.

- Holtzman, B. K., and D. L. Kohlstedt (2007), Stress-driven melt segregation and strain partitioning in partially molten rocks: Effects of stress and strain, *J. Petrol.*, *48*, 2379–2406, doi:10.1093/petrology/egm065.
- Kanamori, H., and F. Press (1970), How thick is the lithosphere?, *Nature*, *226*, 330–331, doi:10.1038/226330a0.
- Kanazawa, T., H. Shiobara, M. S. M. Mochizuki, and E. Araki (2001), Seismic observation system on the sea floor, in *Workshop Report of OHP/ION Joint Symposium, Long-Term Observations in the Oceans*, pp. S11–6, Earthquake Res. Inst., Univ. of Tokyo, Tokyo.
- Karato, S., and H. Jung (1998), Water, partial melting and the origin of the seismic low velocity and high attenuation zone in the upper mantle, *Earth Planet. Sci. Lett.*, *157*, 193–207, doi:10.1016/S0012-821X(98)00034-X.
- Kawakatsu, H., P. Kumar, Y. Takei, M. Shinohara, T. Kanazawa, E. Araki, and K. Suyehiro (2009a), Seismic evidence for sharp lithosphere-asthenosphere boundaries of oceanic plates, *Science*, *324*, 499–502.
- Kawakatsu, H., A. Takeo, Y. Takei, and P. Kumar (2009b), Seismological consequences and observability of melt-lubricated (millefeuille) asthenosphere and a LAB above, *Eos Trans. AGU*, *90*(52), Fall Meet. Suppl., Abstract D111A-03.
- Kennett, B. L. N., and E. R. Engdahl (1991), Travel times for global earthquake location and phase identification, *Geophys. J. Int.*, *105*, 429–465, doi:10.1111/j.1365-246X.1991.tb06724.x.
- Kumar, M. R., and M. G. Bostock (2008), Extraction of absolute velocity from receiver functions, *Geophys. J. Int.*, *175*, 515–519, doi:10.1111/j.1365-246X.2008.03963.x.
- Kumar, P., and H. Kawakatsu (2011), Imaging the seismic lithosphere-asthenosphere boundary of the oceanic plate, *Geochem. Geophys. Geosyst.*, *12*, Q01006, doi:10.1029/2010GC003358.
- Kumar, P., X. Yuan, R. Kind, and G. Kosarev (2005a), The lithosphere-asthenosphere boundary in the Tien Shan-Karakoram region from S receiver functions: Evidence for continental subduction, *Geophys. Res. Lett.*, *32*, L07305, doi:10.1029/2004GL022291.
- Kumar, P., et al. (2005b), The lithosphere asthenosphere boundary in the North-West Atlantic region, *Earth Planet. Sci. Lett.*, *236*, 249–257, doi:10.1016/j.epsl.2005.05.029.
- Kumar, P., X. Yuan, R. Kind, and J. Ni (2006), Imaging the colliding Indian and Asian lithospheric plates beneath Tibet, *J. Geophys. Res.*, *111*, B06308, doi:10.1029/2005JB003930.
- Kumar, P., X. Yuan, M. Ravi Kumar, R. Kind, X. Li, and R. K. Chadha (2007), The rapid drift of the Indian tectonic plate, *Nature*, *449*, 894–897, doi:10.1038/nature06214.
- Kumar, P., R. Kind, and X. Yuan (2010), Receiver function summation without deconvolution, *Geophys. J. Int.*, *180*, 1223–1230, doi:10.1111/j.1365-246X.2009.04469.x.
- Landes, M., J. R. Ritter, and P. W. Readman (2007), Proto-Iceland plume caused thinning of Irish lithosphere, *Earth Planet. Sci. Lett.*, *225*, 32–40.
- Langston, C. A. (1977), Corvallis, Oregon, crustal and upper mantle structure from teleseismic P and S waves, *Bull. Seismol. Soc. Am.*, *67*, 713–724.
- Langston, C. A., and J. K. Hammer (2001), The vertical component P-wave receiver function, *Bull. Seismol. Soc. Am.*, *91*, 1805–1819, doi:10.1785/0120000225.
- Leeds, A. R., L. Knopoff, and E. G. Kausel (1974), Variations of upper mantle structure under the Pacific Ocean, *Science*, *186*, 141–143, doi:10.1126/science.186.4159.141.
- Li, X., R. Kind, X. Yuan, I. Wölber, and W. Hanka (2004), Rejuvenation of the lithosphere by the Hawaiian plume, *Nature*, *427*, 827–829, doi:10.1038/nature02349.
- Nettles, M., and A. M. Dziewonski (2008), Radially anisotropic shear velocity structure of the upper mantle globally and beneath North America, *J. Geophys. Res.*, *113*, B02303, doi:10.1029/2006JB004819.
- Oliver, J. (1962), A summary of observed seismic surface wave dispersion, *Bull. Seismol. Soc. Am.*, *52*, 81–86.
- Priestley, K., and D. McKenzie (2006), The thermal structure of the lithosphere from shear wave velocities, *Earth Planet. Sci. Lett.*, *244*, 285–301, doi:10.1016/j.epsl.2006.01.008.
- Raitt, R. W. (1963), The crustal rocks, in *The Sea*, vol. 3, edited by M. N. Hill, pp. 85–102, Wiley-Interscience, New York.
- Raitt, R. W., G. G. Shor Jr., T. J. G. Francis, and G. B. Morris (1969), Anisotropy of the upper mantle, *J. Geophys. Res.*, *74*, 3095–3109, doi:10.1029/JB074i012p03095.
- Revenaugh, J., and T. H. Jordan (1991a), Mantle layering from reverberations: 2. The transition zone, *J. Geophys. Res.*, *96*, 19,763–19,780, doi:10.1029/91JB01486.
- Revenaugh, J., and T. H. Jordan (1991b), Mantle layering from reverberations: 3. The upper mantle, *J. Geophys. Res.*, *96*, 19,781–19,810, doi:10.1029/91JB01487.
- Richards, P. G. (1972), Seismic waves reflected from velocity gradient anomalies within the Earth's upper mantle, *J. Geophys.*, *38*, 517–527.
- Rychert, C. A., and P. M. Shearer (2009), A global view of the lithosphere-asthenosphere boundary, *Science*, *324*, 495–498, doi:10.1126/science.1169754.
- Rychert, C. A., and P. M. Shearer (2011), Imaging the lithosphere-asthenosphere boundary beneath the Pacific using SS waveform modeling, *J. Geophys. Res.*, *116*, B07307, doi:10.1029/2010JB008070.
- Rychert, C. A., S. Rondenay, and K. M. Fischer (2007), P-to-S and S-to-P imaging of a sharp lithosphere-asthenosphere boundary beneath eastern North America, *J. Geophys. Res.*, *112*, B08314, doi:10.1029/2006JB004619.
- Salisbury, M. H., et al. (2002), *Proceedings of the Ocean Drilling Program Initial Reports*, vol. 195, Ocean Drill. Program, College Station, Tex., doi:10.2973/odp.proc.ir.195.2002.
- Shearer, P. M. (1991), Imaging global body wave phases by stacking long-period seismograms, *J. Geophys. Res.*, *96*, 20,353–20,364, doi:10.1029/91JB00421.
- Shearer, P. M., and J. A. Orcutt (1986), Compressional and shear wave anisotropy in the oceanic lithosphere—The Ngendei seismic refraction experiment, *Geophys. J. R. Astron. Soc.*, *87*, 967–1003.
- Shimamura, H., and T. Asada (1984), Velocity anisotropy extending over the entire depth of the oceanic lithosphere, in *Geodynamics of the Western Pacific-Indonesian Region, Geodynamics Ser.*, vol. 11, edited by T. W. C. Hilde and S. Uyeda, pp. 121–125, AGU, Washington, D. C.
- Shinohara, M., E. Araki, T. Kanazawa, K. Suyehiro, M. Mochizuki, T. Yamada, K. Nakahigashi, Y. Kaiho, and Y. Fukao (2006), Deep-sea borehole seismological observatories in the western Pacific: Temporal variation of seismic noise level and event detection, *Ann. Geophys.*, *49*, 625–642.
- Shinohara, M., T. Fukano, T. Kanazawa, E. Araki, K. Suyehiro, M. Mochizuki, K. Nakahigashi, T. Yamada, and K. Mochizuki (2008), Upper mantle and crustal seismic structure beneath the Northwestern Pacific Basin using seafloor borehole broadband seismometer and ocean bottom seismometers, *Phys. Earth Planet. Inter.*, *170*, 95–106, doi:10.1016/j.pepi.2008.07.039.
- Shiobara, H., K. Baba, H. Utada, and Y. Fukao (2009), Ocean bottom array probes stagnant slab beneath the Philippine Sea, *Eos Trans. AGU*, *90*(9), 70–71, doi:10.1029/2009EO090002.
- Soudouji, F., R. Kind, D. Hatzfeld, K. Priestley, W. Hanka, K. Wylegalla, G. Stavrakakis, A. Vafidis, H.-P. Harjes, and M. Bohnhoff (2006), Lithospheric structure of the Aegean obtained from P and S receiver functions, *J. Geophys. Res.*, *111*, B12307, doi:10.1029/2005JB003932.
- Spudich, P., and J. Orcutt (1980), A new look at the seismic velocity structure of the oceanic crust, *Rev. Geophys.*, *18*, 627–645, doi:10.1029/RG018i003p00627.
- Suetsugu, D., et al. (2005), Mantle discontinuity depths beneath the West Philippine Basin from receiver function analysis of deep-sea borehole and seafloor broadband waveforms, *Bull. Seismol. Soc. Am.*, *95*, 1947–1956, doi:10.1785/0120040169.
- Tan, Y., and D. V. Helmberger (2007), Trans-Pacific upper mantle shear velocity structure, *J. Geophys. Res.*, *112*, B08301, doi:10.1029/2006JB004853.
- Vinnik, L. P. (1977), Detection of waves converted from P-to-SV in the mantle, *Phys. Earth Planet. Inter.*, *15*, 39–45, doi:10.1016/0031-9201(77)90008-5.
- Wessel, P., and W. H. F. Smith (1995), New version of the Generic Mapping Tools released, *Eos Trans. AGU*, *76*, 33, doi:10.1029/95EO00198.
- White, R., D. McKenzie, and R. O'Nions (1992), Oceanic crustal thickness from seismic measurements and rare Earth element inversions, *J. Geophys. Res.*, *97*, 19,683–19,715, doi:10.1029/92JB01749.
- Yuan, X., J. Ni, R. Kind, J. Mechie, and E. Sandvol (1997), Lithospheric and upper mantle structure of southern Tibet from a seismological passive source experiment, *J. Geophys. Res.*, *102*, 27,491–27,500, doi:10.1029/97JB02379.
- Yuan, X., R. Kind, X. Li, and R. Wang (2006), The S receiver functions: Synthetics and data example, *Geophys. J. Int.*, *165*, 555–564, doi:10.1111/j.1365-246X.2006.02885.x.
- Zhang, Y.-S., and T. Tanimoto (1993), High-resolution global upper mantle structure and plate tectonics, *J. Geophys. Res.*, *98*, 9793–9823, doi:10.1029/93JB00148.

E. Araki and K. Suyehiro, Japan Agency for Marine-Earth Science and Technology, 2-15 Natsushima, Yokosuka 237-0061, Japan.

T. Kanazawa, H. Kawakatsu, P. Kumar, and M. Shinohara, Earthquake Research Institute, University of Tokyo, 1-1-1 Yayoi, Bunkyo-ku, Tokyo 113-0032, Japan. (prakashk@ngri.res.in)